International Journal of Heat and Mass Transfer 186 (2022) 122501

Contents lists available at ScienceDirect

International Journal of Heat and Mass Transfer

journal homepage: www.elsevier.com/locate/hmt

# Learning new physical descriptors from reduced-order analysis of bubble dynamics in boiling heat transfer

Arif Rokoni[a], Lige Zhang[a], Tejaswi Soori[a], Han Hu[b], Teresa Wu[c], Ying Sun[a,*]

[a] Department of Mechanical Engineering and Mechanics, Drexel University, Philadelphia, PA 19104, USA
[b] Department of Mechanical Engineering, University of Arkansas, Fayetteville, AR, 72701, USA
[c] School of Computing, Informatics, and Decision Systems Engineering, Arizona State University, Tempe, AZ 85281, USA

ARTICLE INFO

*Article history:*
Received 2 October 2021
Revised 13 December 2021
Accepted 28 December 2021

*Keywords:*
Machine learning
Pool boiling
Reduced-order analysis
Critical heat flux
Future prediction

ABSTRACT

Understanding bubble dynamics during boiling is challenging due to the drastic changes in system parameters, such as nucleation, bubble morphology, temperature, and pressure. In this study, principal component analysis (PCA), an unsupervised dimensionality reduction algorithm, is used to extract new physical descriptors of boiling heat transfer from pool boiling experimental images without labeling and training. The dominant frequency and amplitude of the time-series principal components (PCs) are analyzed, where the first few dominant PCs are used to approximate the instantaneous bubble morphologies, drastically reducing the data dimensions. The results show that the dominant frequency and amplitude can be used as new physical descriptors to distinguish different boiling regimes. The dominant frequency of the first PC is found to increase with heat flux in the discrete bubble regime until it reaches a peak and then decreases with heat flux in the bubble interference and coalescence regime, where the former is believed to be associated with the increase in bubble nucleation sites and the latter is associated with the bubble coalescence during pool boiling. The dominant frequency and amplitude extracted from the present unsupervised learning are qualitatively compared to the bubble count and size extracted from a supervised deep-learning algorithm, and the approach appears highly robust over multiple datasets and heater surfaces. To predict future boiling states for mitigating boiling crises, bidirectional long short-term memory (BiLSTM) neural network is used to estimate the future variations of PCs and hence the bubble dynamics, from time-series PCs. The PCA-BiLSTM models predict reduced-order bubble images well and show significantly higher prediction accuracy compared to the Convolutional-LSTM.



## 1. Introduction

Boiling is an important heat transfer process in thermoelectric power plants [1], water purification [2], refrigeration and air conditioning [3], thermal management of high-performance electronics [4,5], data centers [6], nuclear reactors [7], and other energy-intensive industrial processes. Boiling is a stochastic process dependent on parameters such as the heater surface superheat, wettability and roughness, dissolved gas concentration, working fluid subcooling, operating pressure, and heating patterns. The high heat transfer rate in the nucleate boiling (NB) regime is bound by its upper limit, the critical heat flux (CHF), where an insulating stable vapor layer blankets the entire heater surface and restricts the heat dissipation, leading to a rapid rise in the heater surface temperature above its design limit and causing catastrophic damage to the system, known as the boiling crisis.

Several mechanisms have been proposed to understand the CHF, including the hydrodynamic instabilities [8,9] and the near-surface phenomena [10], such as surface wettability [11–13] and wickability [14–18], vapor recoil-induced contact angle change [19,20], bubble growth time and departure frequency [21,22], contact line density [23], and continuum percolation based on near-wall stochasticity [24]. One of the biggest challenges facing boiling heat transfer is the precursor mechanism that triggers the CHF, which has remained elusive despite extensive research over the past several decades [25–27]. Complex bubble dynamics and their correlation to the heat flux are crucial for a better understanding of boiling mechanisms, thus, to accurately predict CHF and its enhancement. Existing analytical and computational methods to predict the boiling process or estimate the heat flux are either computationally expensive or lack accuracy due to the chaotic nature of the boiling process [28–30]. Presently, boiling heat transfer still requires experimental measurements and correlations to estimate heat fluxes, especially the CHF [31]. However, the majority of the correlations differ from each other and are often specific to the

* Corresponding author.
*E-mail address:* ys347@drexel.edu (Y. Sun).

https://doi.org/10.1016/j.ijheatmasstransfer.2021.122501
0017-9310/

heater surfaces and operating conditions [32–35]. Thus, there is a lack of a general model to predict CHF irrespective of working fluids, operating conditions, and heater surfaces. Due to the highly unpredictable nature of CHF [36], the common practice to avoid the boiling crisis is to operate the system well below the CHF limit [37,38]. Current sensor-based approaches can only identify boiling crises a posteriori, leading to overheating and system failures. Accurate real-time prediction of CHF enables reliable near-CHF operations and hence increases the energy efficiency of boiling processes.

Machine learning (ML) has been applied to boiling studies in recent years, from detecting flow boiling regimes, the onset of film boiling, CHF, and departure from nucleate boiling, to estimating boiling heat flux, heat transfer coefficient, nucleation site density, and bubble statistics [39–55]. The supervised learning approaches in the past have used artificial neural networks (ANN) [42,44,48,49,51-55], support vector machines (SVM) [39], and convolutional neural networks (CNN) [40,41,43,45,46] to perform boiling image classification based on boiling regimes. The use of unsupervised learning approaches such as principal component analysis [39,41,45] has been limited to performing data-driven clustering of boiling images based on boiling regimes, however, the results showed a lack of interpretability. Suh et al. [43] used hybrid deep learning models to replace image analysis to extract features, such as bubble size and counts, and to correlate high-resolution bubble dynamics with the associated boiling curves. Ravichandran and Bucci quantified the bubble growth time, departure frequency, and nucleation site density using a single layer, feed-forward ANN, trained using high-speed infrared (IR) data from pool boiling experiments of water on plain and nanostructured surfaces [42] and demonstrated that boiling is a near-wall phenomenon where surface wickability modifies bubble dynamics [44]. Sinha et al. used the acoustic emission (AE) spectrograms to train a CNN model that can predict the boiling regimes despite the variations in boiling surfaces, working fluids, and heating strategies [46], where a shift in the peak frequency occurs when the boiling regime transitions from NB to CHF. Recently, we have used transfer learning (TL) to increase the generality of the deep learning (DL) model [45] to successfully predict boiling regimes on cross-domain datasets.

Data-driven DL approach has been heralded as an alternative to the conventional physics-based approach, but so far, its success has been mainly limited to diagnostic and prognostic purposes. The possibility of using deep neural networks trained using experimental and/or computational data to either extract, explain, or infer (or all three together) some form of physical understanding of the complex boiling heat transfer phenomena albeit very promising, the amount of progress in terms of applying DL to obtain interpretable physical and mathematical insights has been limited. Moreover, the use of DL beyond the task of classification has also not been fully explored in past studies.

Principal component analysis (PCA) is an unsupervised dimensionality reduction algorithm to describe correlations in high-dimensional data [56] and can be used as a versatile tool to determine low-dimensional representations of high-dimensional images while extracting dominant variations and patterns. PCA shows promise in complex fluid systems, weather prediction, turbulence modeling, and computer vision applications [57–62]. Recently, PCA has been used to extract vortex shedding frequency and dominant modes using correlations between purely visualization-based images and particle image velocimetry (PIV) measurements [63]. In the present study, PCA is used to extract dominant low-dimensional features from in-house pool boiling experimental images to obtain physically interpretable descriptors of bubble dynamics versus heat flux in boiling heat transfer processes.

Fig. 1 shows the schematic of recently reported supervised [43] (top row) and current unsupervised (bottom row) ML approaches of determining physically interpretable descriptors governing the bubble dynamics. The supervised approach is an image segmentation-based ML (e. g., Mask R-CNN [43]) which extracts bubble statistics (e.g., bubble size and count) based on manual tagging of bubble size and count, where each image is labeled with its associated heat flux value. The manual tagging involved with the supervised ML of the training datasets leads to potential human errors especially for boiling images with vigorous bubble interference and coalescence events occurring at higher heat flux values. Our unsupervised, PCA-based ML approach works by separating the significant features from the insignificant parts such as the heater and stationary bubbles in each image, thereby enabling direct quantification of bubble dynamics related descriptors such as dominant frequency and amplitude of principal components (PCs) versus heat flux, independent of the vigorous bubble interference and coalescence events. Additionally, the results obtained from PCA can be interpreted easily and qualitatively explained based on the bubble morphologies and show higher accuracy when compared with the state-of-the-art image segmentation-based ML, such as Mask R-CNN, thereby providing a robust unsupervised ML tool for analyzing two-phase heat transfer processes.

Early detection of boiling crises is crucial for safety protocols such as heater shut-off and coolant pump activation in thermal power systems such as high-pressure boilers and nuclear reactors, where the total duration of prediction is important to activate boiling crisis mitigation strategies. Image-based recurrent neural networks, such as Convolutional-Long Short-Term Memory (Conv-LSTM), that are trained on recognizing time-dependent patterns in data have been proposed in the past to predict future events, albeit with limited success due to such methods being inadequate to filter significant features from insignificant ones that contribute to prediction errors. Due to the prediction errors, Conv-LSTM has been successful only in predicting a few future image frames [64]. In general, convolution-based models tend to focus on spatial appearances and are weak in predicting long-term temporal dependency [65,66]. To enable fast and accurate real-time prediction of future bubble dynamics, a bidirectional long short-term memory (BiLSTM) model is trained in this study using reduced-order representations of the bubble morphology. As shown in Fig. 2, the first few PCs versus time data are used to train the BiLSTM DL model and the predicted future PC variations are used to reconstruct the reduced-order bubble images. The BiLSTM network, with the ability to recognize patterns in sequential data which are then used to predict the future instances [67–71], has been implemented to reconstruct unsteady [70] and turbulent flows [68,69], as well as fast prediction of accidents in nuclear power plants, based on simulated data [72].

In this study, PCA is used to extract new physical descriptors from reduced-order representations of the pool boiling images. The 1st PC versus time data is analyzed using fast-Fourier transform (FFT) to extract dominant frequencies and amplitude versus heat flux values. The frequency and amplitude results obtained from the unsupervised PCA approach are then qualitatively compared to the bubble count and size results obtained from the supervised image segmentation ML algorithm, Mask R-CNN. Next, an effort is made to physically interpret the unsupervised ML results for different boiling regimes by analyzing the trends seen in dominant frequency and amplitude versus heat flux data. The robustness of the PCA approach is verified on datasets obtained from multiple domains (pool boiling images from in-house experiments and publicly available YouTube videos) where the dominant frequency and amplitude trends are used to distinguish the CHF regime from the NB regime. Separately, the time-dependent PCs are used as inputs for the BiLSTM ML network to predict future PC versus time data which are then reconstructed into reduced-order bubble images and the PCA-BiLSTM performance is compared with Conv-LSTM

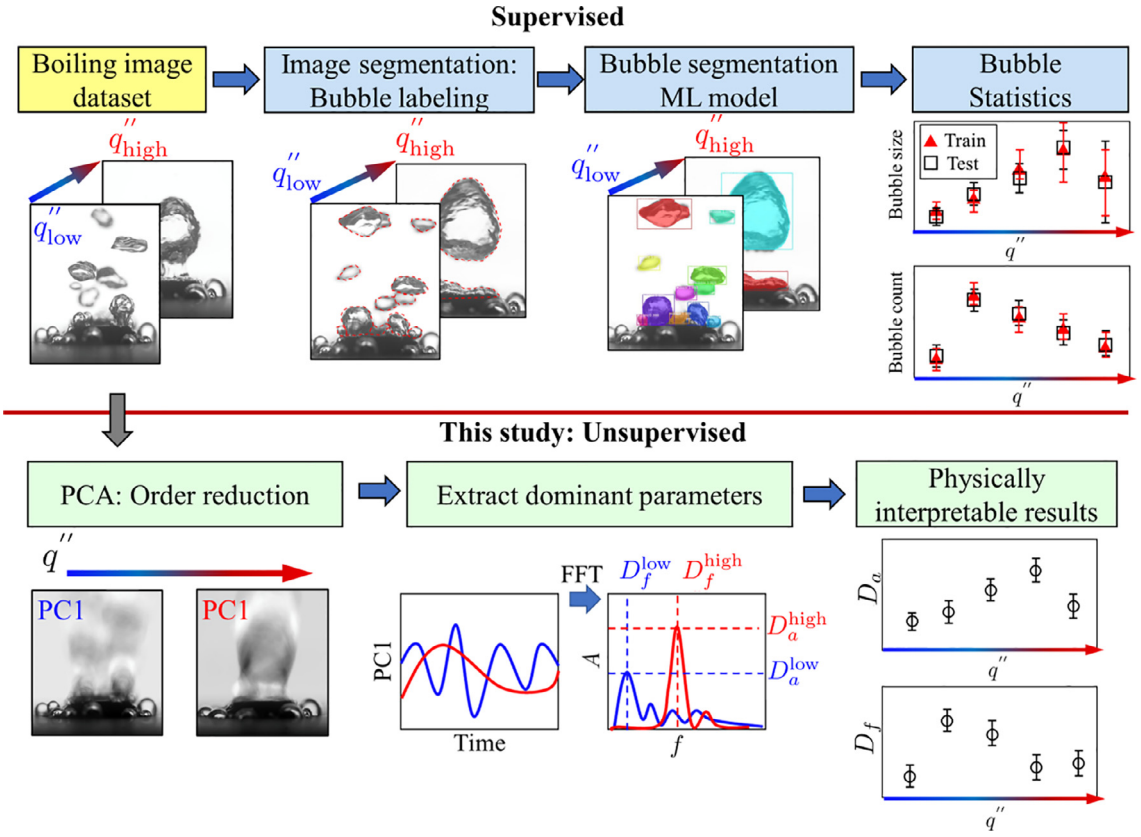


**Fig. 1.** Comparison of a supervised ML approach to extract bubble statistics and the current unsupervised ML approach to extract physically interpretable descriptors from reduced-order bubble dynamics, at different heat loads. Here, $q''$, PC1, FFT, $f$, $D_f$, $A$, and $D_a$ are heat flux, 1st principal component, fast Fourier transform, frequency, dominant frequency, amplitude, and dominant amplitude, respectively.

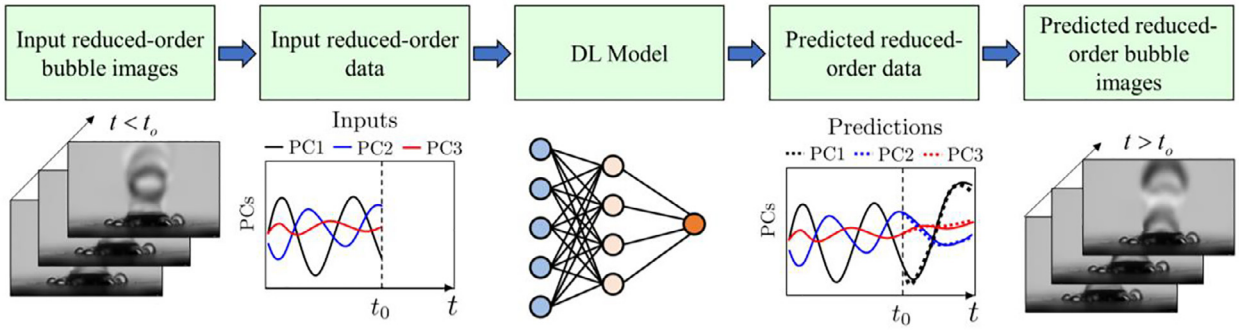


**Fig. 2.** Schematics of PCA-BiLSTM framework for predicting future reduced-order bubble images. The bubble morphologies for a range of heat fluxes are analyzed using PCA to reduce the dimensionality. The time-series of PCs from reduced-order modeling is fed to the BiLSTM DL network to predict the future time-series of PCs which are then used to reconstruct bubble morphologies. The flowchart of the top panel illustrates the PCA-BiLSTM approach: PCA reduces the order of boiling images for $t < t_o$, BiLSTM takes the output from PCA to learn and predict the reduced-order PCs for $t > t_o$, and the predicted reduced-order PCs are used for future prediction of bubble morphologies.

which uses full-resolution images. Finally, we show that the current PCA-BiLSTM approach can successfully predict future reduced-order bubble images with as few as 10 PCs in comparison to the Conv-LSTM which requires full-resolution images containing millions of pixels, thereby enabling future developments into fast and real-time DL prediction tools.

## 2. Methods and procedures

### 2.1. Pool boiling experiments

The in-house pool boiling experiments were performed on a plain square copper heater with a surface area of 100 mm$^2$, and water was used as the working fluid. The heater surface was polished with 320-grit sandpaper followed by 600-grit sandpaper prior to experiments. The boiling images were captured using a high-speed camera (Phantom VEO-710) at 1000 fps with a resolution of 1280 × 800 for a range of steady-state heat fluxes from 2.9 W/cm$^2$ to 109.9 W/cm$^2$ and at CHF. All experiments were performed at steady-state conditions under an ambient pressure of 1 atm. T-type thermocouples were used for temperature measurements, which leads to heat flux calculations. A pool boiling experiment was also performed using a transient heat load where the heat flux was increased from 22.1 W/cm$^2$ to 53.1 W/cm$^2$ over a period of 50 s and the corresponding bubble images were captured at 500 fps with a resolution of 600 × 832. A total of 25,000 frames corresponding to 50 s data was captured for the study. Apart from the plain copper surface, in-house pool boiling experi-

ments were also performed on copper foam surface fabricated via cathodic electrodeposition with a deposition time of 360 s. Additionally, publicly available pool boiling videos [73] were also used to verify the robustness of the current ML method. Pool boiling videos from YouTube contain bubble visualizations for a range of heat fluxes, from 0.5 W/cm$^2$ to 100 W/cm$^2$, and CHF. The YouTube videos also contain bubble visualizations for different heater surfaces, such as microporous coated copper heater and plain copper heater. The square heaters had a surface area of 100 mm$^2$, and water was used as the working fluid. The resolution of the video frames was 512 × 480 with a frame rate of 2000 fps [74].

### 2.2. PCA of pool boiling images

PCA is a widely used [57–62] statistical dimensionality reduction technique [75]. The essence of PCA is to transform the data to new orthogonal coordinate systems, where the first new coordinate axis represents the largest variance in the original data, the second axis represents the second largest variance, and so on. For original data, consisting of $p$ variables and $n$ observations, $p$ new coordinate axes can be constructed. The first few coordinate axes encode the most significant variances or features of the original data, whereas the latter ones correspond to noises/insignificant variances. In short, PCA transforms a set of correlated variables into a small set of uncorrelated variables, named principal components (PCs). Consider a dataset $\boldsymbol{X}$ of size $p \times n$, consisting of $p$ variables and $n$ observations. For a sequence of images captured during a pool boiling experiment, $p$ is the total number of pixels of each image and $n$ is the total number of images. For example, for a frame rate of 1000 frames per second (fps), images acquired over 5 s lead to $n = 5000$. The mean value of each row in $\boldsymbol{X}$ is calculated as, $\bar{x}_i = \frac{1}{n}\sum_{j=1}^{n} \boldsymbol{X}_{ij}$, where $i = 1, 2, 3, \ldots, p$. The mean matrix $\bar{\boldsymbol{X}} = \bar{\boldsymbol{x}}\boldsymbol{Q}$, where $\bar{\boldsymbol{x}}$ has a size of $p \times 1$ with elements $\bar{x}_i$ and $\boldsymbol{Q}$ is $1 \times n$with all elements of 1. The mean-subtracted matrix $\boldsymbol{B} = \boldsymbol{X} - \bar{\boldsymbol{X}}$ and its transpose $\boldsymbol{A} = \boldsymbol{B}^T$ of size $n \times p$ can be decomposed as $\boldsymbol{A} = \boldsymbol{U}\sum\boldsymbol{V}^T$ using the singular value decomposition (SVD) technique [76]. Here, $\boldsymbol{U}$ and $\boldsymbol{V}$ are unitary matrices ($\boldsymbol{U}^T\boldsymbol{U} = \boldsymbol{U}\boldsymbol{U}^T = \boldsymbol{I}$ and $\boldsymbol{V}^T\boldsymbol{V} = \boldsymbol{V}\boldsymbol{V}^T = \boldsymbol{I}$) of size $n \times n$ and $p \times p$, respectively. The columns of $\boldsymbol{V}$ are the eigenvectors of the covariance matrix, $\boldsymbol{C} = \boldsymbol{A}^T\boldsymbol{A}$, and $\sum$ is the rectangular diagonal matrix of size $n \times p$, containing eigenvalues of $\boldsymbol{C}$ in descending order. The PCs, $\boldsymbol{T}$, are the projection of $\boldsymbol{A}$ onto the eigenvectors, $\boldsymbol{V}$, such that $\boldsymbol{T} = \boldsymbol{A}\boldsymbol{V}$. The entire dataset consists of $p$ number of PCs, but the high-dimensional dataset can be represented using the first $q$ PCs where $q << p$. Then, the first $q$ number of PCs are calculated using, $\boldsymbol{T}_q = \boldsymbol{A}\boldsymbol{V}_q$, where $\boldsymbol{T}_q$, $\boldsymbol{A}$, and $\boldsymbol{V}_q$ are matrices of size $n \times q$, $n \times p$, and $p \times q$. For example, when $q = 5$, $\boldsymbol{T}_5$ is a matrix of size $n \times 5$ consisting of the first 5 PCs. The original data, $\boldsymbol{X}$, can then be approximated in a reduced-order form, $\boldsymbol{X}_{\boldsymbol{R}}$, using the first $q$ PCs, $\boldsymbol{T}_q$, as $\boldsymbol{X}_{\boldsymbol{R}} = \boldsymbol{A}_{\boldsymbol{R}}^T + \bar{\boldsymbol{X}}$, where $\boldsymbol{A}_{\boldsymbol{R}} = \boldsymbol{T}_q\boldsymbol{V}_q^T$ since $\boldsymbol{V}_q$ is a unitary matrix. Each column within the original data and its reduced-order representation correspond to an image at a given time $t$, and hence the time-series of the reduced-order data can be expressed as $\boldsymbol{X}_{\boldsymbol{R}}(t) = \boldsymbol{A}_{\boldsymbol{R}}{}^T(t) + \bar{\boldsymbol{X}}$.

In this study, PCA was performed on pool boiling images. Individual frames were extracted from the videos captured during the in-house pool boiling experiments and using MATLAB code via the VideoReader and imwrite functions for the publicly available YouTube videos [73]. Duplicate frames during the extraction process from the YouTube videos were removed by calculating the relative difference using the Structural Similarity Index (SSIM), where consecutive images with a relative difference of less than 0.03% were removed. Time-series PCs were calculated from the sequential images. Fig. 3a shows a boiling image taken from an in-house pool boiling experiment at CHF with a resolution of 1280 × 800, or 1024,000 components, as well as the reconstructed images using the first 1, 5, 10, 50, and 100 PCs. The images reconstructed from the first ten and more PCs can capture well the bubble shape and position, key information for extracting the bubble dynamics. Fig. 3b shows the percentage of explained variance with respect to the rank of the PCs, where 20% of variances are captured by the 1st PC, 16% of variances are captured by the 2nd PC, and so on. Higher rank PCs capture only a small number of variances; for example, PC 10 and higher ones only capture variances. The variables to represent bubble morphologies can be reduced from 1024,000 to 10, which is advantageous when dealing with a large number of time-series data or for high-speed dynamical systems. To encode the dynamic nature of bubble morphologies, time-series PCs were calculated using boiling images captured at 1000 fps. The first 10 PCs were found to contain 70.7% of cumulative explained variance pertaining to the bubble shape and position, and were hence calculated for the time-series data. Fig. 3c shows the variation of PC1 (black), PC3 (blue), and PC5 (red) versus time.

### 2.3. PCA-BiLSTM for future prediction

Long Short-Term Memory (LSTM), a type of Recurrent Neural Network (RNN) [77] specialized to process sequential data, is capable of learning long-term temporal dependencies [78–81]. The major advantage of LSTM is its ability to handle gradient explosion or disappearance issues [82]. Fig. 4a shows a representative LSTM unit with four interacting neural network layers, 3 sigmoid and 1 hyperbolic tangent (tanh) dense layer. The current timestep takes the input data and information from the previous timestep and calculates the output and information for the next timestep. LSTM has the unique ability to remove or add information to the cell state, $C$, through the well-structured forget and input gates, which consist of interacting neural network layers. As shown in Fig. 4a, $\sigma$ is the sigmoid layer, where the output varies between 0 and 1, which acts as a memory to forget or remember, respectively. The forget gate of the LSTM unit takes the hidden state from the previous timestep, $h_{t-1}$, and the input data for the current timestep, $x_t$, and outputs a value between 0 and 1. The output from the forget gate is multiplied with the cell state from the previous timestep, $C_{t-1}$, to remove less relevant information. The input gate decides which information to be stored in the cell state. The multiplication of the outputs from the sigmoid and tanh layers is added to the cell state. The cell state, $C$, undergoes removal and addition of information and thus holds the long-term dependencies and solves the gradient explosion or disappearance issue. Here, $C_{t-1}$ is the cell state from the previous timestep and $C_t$ is the updated cell state from the current timestep. The output gate takes the tanh of cell state, $C_t$, and multiplies it with the output from the sigmoid layer to get the output of the current timestep, $h_t$, which acts as the hidden state for the next timestep. As shown in Fig. 4b, Bidirectional LSTM (BiLSTM) [83,84] has two LSTM networks. One is forward and the other is backward direction, as compared to the traditional LSTM where the flow of information is only forward. Bidirectional LSTM has shown improved accuracy for language processing and other related applications [85–88]. In the current study, both LSTM and BiLSTM have been tested and BiLSTM was found to reduce the error in future prediction by 15% over the traditional LSTM, as shown in Appendix A.

A Bidirectional LSTM (BiLSTM) model was trained in this study to predict bubble morphologies for pool boiling using the first 10 PCs of the time-series data, extracted using PCA. Out of the total 4,040 ms PC versus time data, the initial 70% data (0 ms to 2,828 ms) was used for training and the remaining 30% data (2,829 ms to 4,040 ms) was used for testing. The entire training dataset consists of several clusters, where each cluster has 300 ms of sequential data points (200 ms input and 100 ms output). The number of time-series clusters was determined from the 2,828 ms

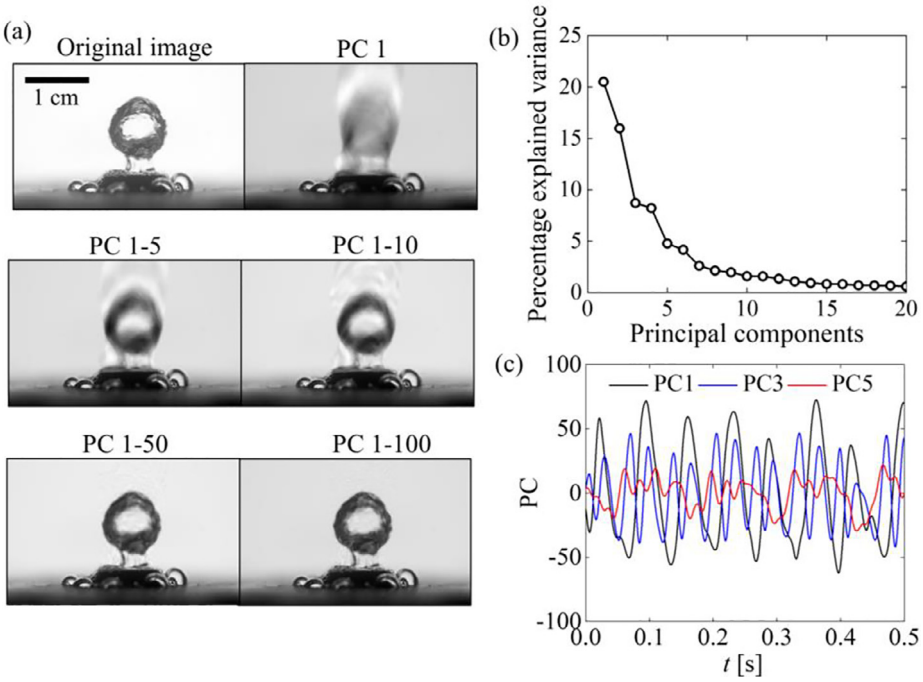


**Fig. 3.** (a) Original image with a resolution of 1280 × 800 (1024,000 components) and reconstructed images using first 1, 5, 10, 50, and 100 principal components, respectively. (b) Percentage of explained variances captured by the principal components. (c) Time-series principal components (1st, 3rd, and 5th PCs), shown for first 0.5 s.

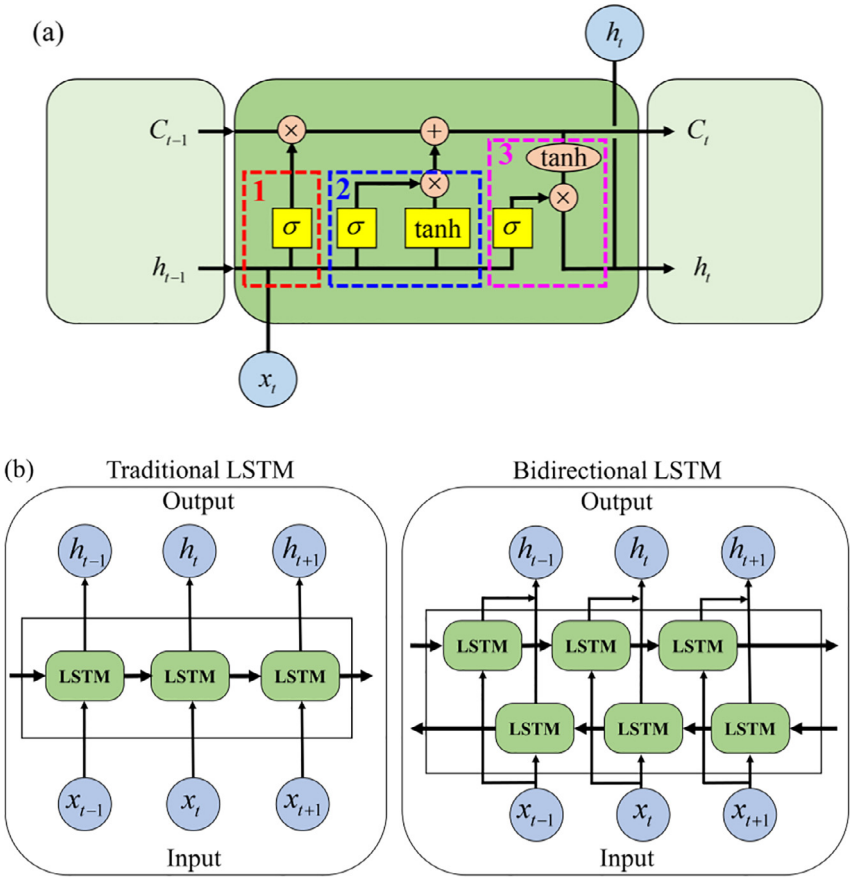


**Fig. 4.** (a) LSTM architecture with forget, input, and output gates marked with red, blue, and purple colors, where the current timestep takes the input data ($x_t$) and information from previous timestep ($C_{t-1}$, $h_{t-1}$) and calculates the output ($h_t$) and information for the next timestep ($C_t$, $h_t$). (b) LSTM and Bidirectional LSTM architectures.

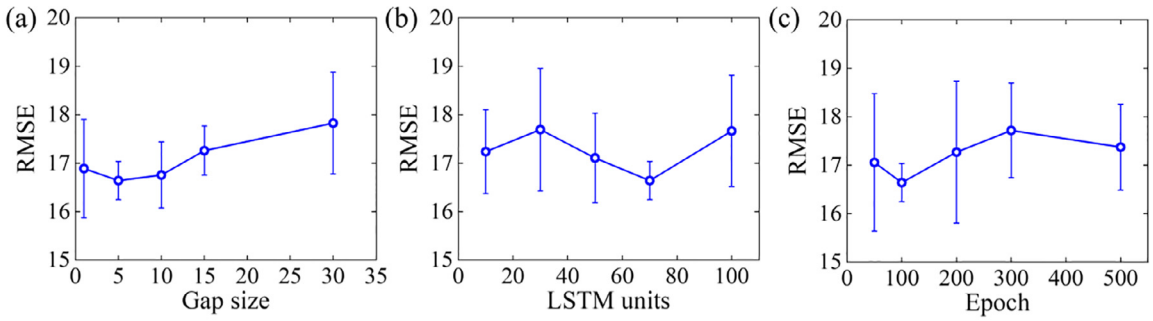


**Fig. 5.** RMSE value with respect to (a) Gap size (70 LSTM units and 100 epochs) (b) LSTM units (5 gap size and 100 epochs) (c) Epoch, (5 gap size and 70 LSTM units) calculated between true and prediction from the testing dataset.

**Table 1**
Hyperparameters used in the BiLSTM model.

| Parameter | Type/Value |
|---|---|
| Optimizer | Adam |
| Learning rate | 0.001 |
| Activation | Sigmoid |
| Regularization | Dropout |
| Loss function | Mean square error |
| Batch size | 1 |
| Validation split | 0.05 |
| Epoch | 100 |

**Table 2**
Model summary of the BiLSTM model.

| Type of layer | Output shape | Parameters |
|---|---|---|
| BiLSTM_1 | (None, 200, 70) | 40,320 |
| Dropout_1 | (None, 200, 70) | 0 |
| BiLSTM_2 | (None, 200, 70) | 78,960 |
| Dropout_2 | (None, 200, 70) | 0 |
| BiLSTM_3 | (None, 200, 70) | 78,960 |
| Dropout_3 | (None, 200, 70) | 0 |
| BiLSTM_4 | (None, 70) | 78,960 |
| Dropout_4 | (None, 70) | 0 |
| Dense | (None, 100) | 7100 |

of training data, depending on the shifting gap. The first cluster used the PC1 data from 0 ms to 200 ms as input and predicted the PC1 data from 201 ms to 300 ms as output. For a shifting gap of 5 ms, the second cluster used the PC1 data from 6 ms to 205 ms as input and predicted the PC1 data from 206 ms to 305 ms, consequently, a total of 506 clusters were used to train the BiLSTM model. The gap size, LSTM units, and epoch of 5, 70, and 100 were selected for the current DL model training from a parameter space of gap size (1, 5, 10, 15, and 30), LSTM units (10, 30, 50, 70, and 100), and epoch (50, 100, 200, 300, and 500) based on the minimum root mean square error (RMSE) value over 10 trials, between true and predicted PC versus time from the testing data, as shown in Fig. 5. Table 1 shows the hyperparameters used in the BiLSTM model training and Table 2 summarizes the BiLSTM model architecture, where the total number of learnable parameters is 78,960. The padding was activated with 1 stride and Sigmoid was selected for activation function. A total of 4 LSTM layers were used, where each layer had 70 units. Each LSTM layer had recurrent activation function followed by a dropout layer with a recurrent dropout of 0.2. The dropout layer turns off 20% of the neurons and is crucial for model generalization. To quantify the stochasticity associated with the DL models, a total of 10 models were trained for each time-series PC data and the best model was selected after calculating the RMSE value between true and prediction PC values from the testing dataset. The trained BiLSTM DL model framework is shown in Fig. 6, where 2827 ms to 3027 ms of PC1 data was used as input to predict 3027 ms to 3127 ms of future PC1 data. The predicted PC1 was compared to the true PC1, as shown in Fig. 6, where blue and red symbols correspond to true and predicted PC1, respectively. The results show good agreement between true and predicted PC1.

## 3. Results and discussion

In this section, PCA and PCA-BiLSTM are examined for extracting new physical descriptors of boiling regimes and future bubble dynamics predictions, respectively. Section 3.1 presents newly identified physical descriptors of boiling regimes obtained using PCA, compared against the conventional descriptors, bubble size and count, obtained using Mark R-CNN, a supervised learning approach. The robustness of the PCA method is demonstrated by analyzing boiling images from both in-house pool boiling experiments and publicly available datasets. Sections 3.2 and 3.3 examine PCA-

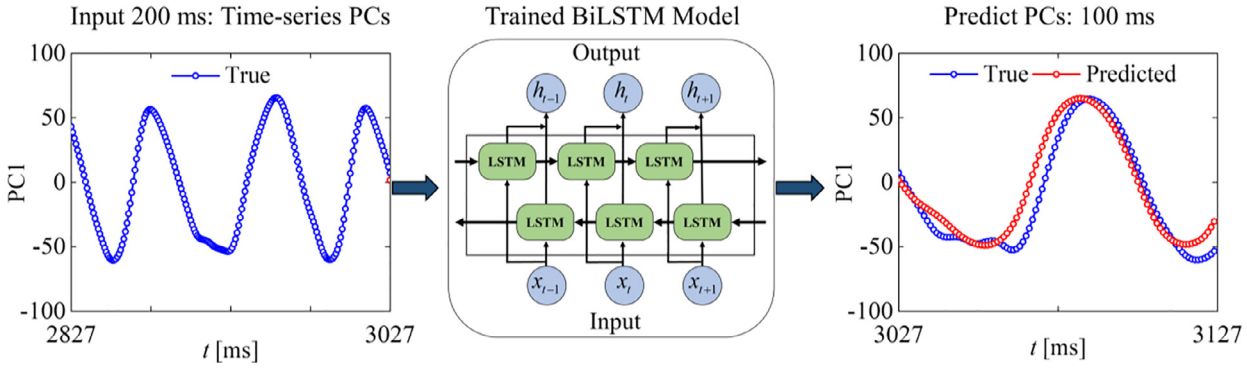


**Fig. 6.** The framework of the trained BiLSTM model for predicting the PC1.

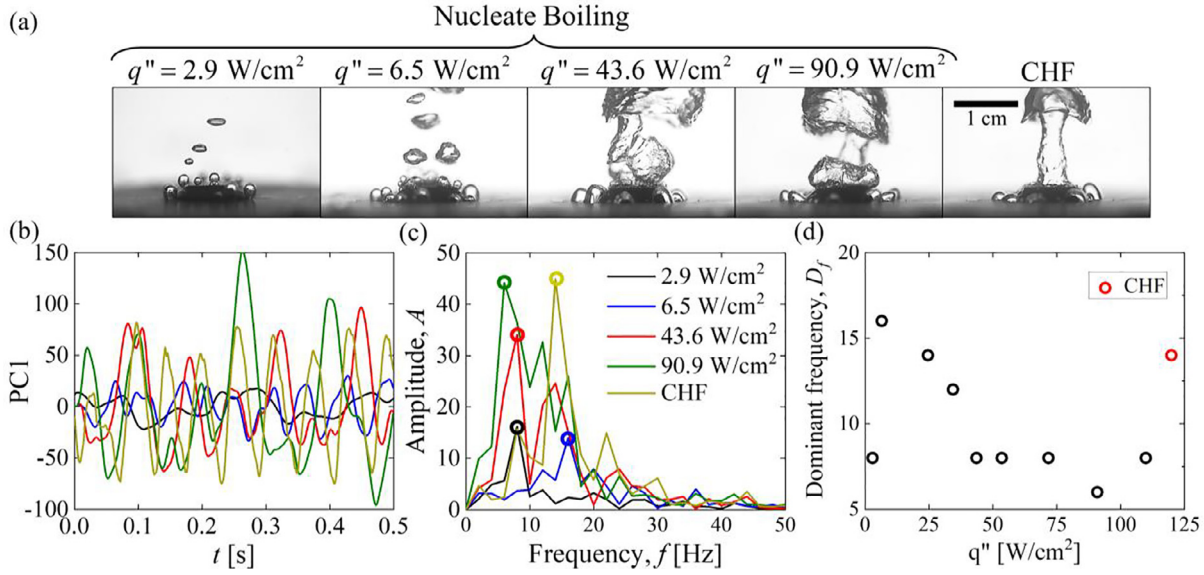


**Fig. 7.** (a) Representative bubble images for a range of heat fluxes during pool boiling, where discrete bubbles are observed for heat flux $\leq$ 6.5 W/cm$^2$ and vigorous bubble coalescence for heat flux $>$ 6.5 W/cm$^2$ within the nucleate boiling regime (b) Time-series 1st principal component, PC1 and (c) Fast Fourier Transform (FFT) of PC1 for five different heat fluxes, 2.9, 6.5, 43.6, 90.9 W/cm$^2$, and CHF for pool boiling on a plain Cu heater. (d) The dominant frequency of PC1, $D_f$, for a range of heat fluxes, 2.9 W/cm$^2$ to CHF.

BiLSTM for the prediction of future boiling frames with a prediction window of 100 ms for steady-state boiling and 60 ms for transient boiling, respectively. Additionally, the results of transient boiling from PCA-BiLSTM are compared against Conv-LSTM, a widely used next-frame prediction algorithm.

### *3.1. Extraction of new physical descriptors of bubble dynamics using PCA*

The PCs of a representative boiling image sequence are analyzed here to extract new physical descriptors of bubble dynamics. Fig. 7a shows representative bubble images for heat flux values of 2.9, 6.5, 43.6, 90.9 W/cm$^2$, and CHF, respectively. Discrete bubbles (DB) for heat flux $\leq$ 6.5 W/cm$^2$, and bubble coalescence and interference (BIC) for heat flux $>$ 6.5 W/cm$^2$, were observed within the nucleate boiling regime. Fig. 7b shows PC1 versus time and Fig. 7c shows the Fast Fourier Transform (FFT) of PC1 versus frequency for heat flux values of 2.9, 6.5, 43.6, 90.9 W/cm$^2$, and CHF, respectively. The amplitude of PC1 varies with frequency at all heat fluxes considered, as shown in Fig. 7c, and the dominant frequency of PC1, marked with colored circles, is dependent on the heat flux. The dominant frequency, $D_f$, varies from 6 to 16 Hz for the heat flux values of 2.9, 6.5, 43.6, 90.9 W/cm$^2$, and CHF, respectively. Fig. 7d shows the dominant frequency, $D_f$, for a range of heat fluxes, 2.9 W/cm$^2$ to CHF, where the dependence of $D_f$ on heat flux is obvious.

To examine the capability of PCA for extracting new physical descriptors from time-series bubble images, Fig. 8 compares the results of PCA against those of Mask R-CNN, a supervised model that was trained to extract the bubble count and size from boiling images of various heat flux values. Mask R-CNN is an image segmentation model [89] and has been used in the past to extract bubble statistics during pool boiling [43] and to locate and measure more than 95% of the bubbles in complex two-phase flows [90]. As a supervised ML model, Mask R-CNN requires manual labeling of data, such as defining the bubble boundaries and numbers, which was done using in-house MATLAB code in the present study. A total of 95 images, taken from a heat flux range of 2.9 W/cm$^2$ to CHF, are used during the training process. Image augmentation technique of flipping, resizing, rotating and Gaussian white noises addition was applied to 50% of the images that are randomly chosen from the dataset to avoid overfitting. The model was trained with a learning rate of 0.001, and up to 600 epochs.

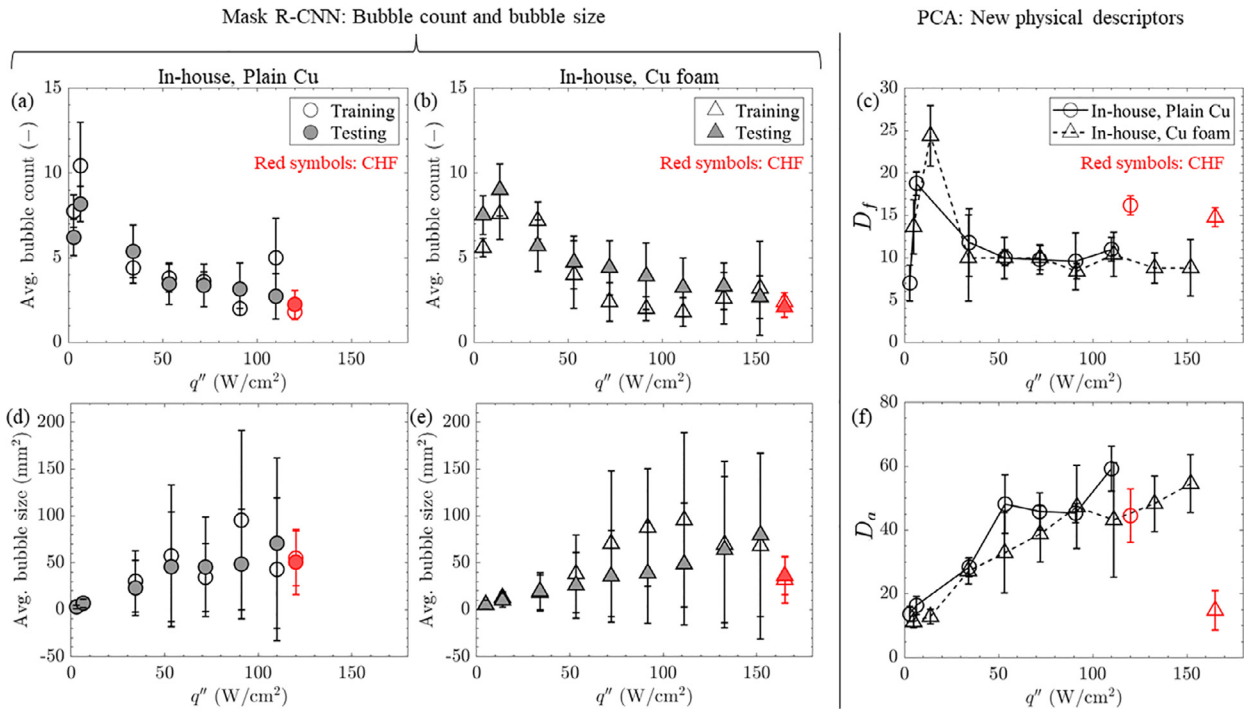


**Fig. 8.** A qualitative comparison of the results obtained from the supervised Mask R-CNN and the unsupervised PCA approach, for the in-house boiling dataset. (a-b, d-e) Bubble count and size calculated using Mask R-CNN with increasing heat flux where (a, d) correspond to in-house plain copper heater surface and (b, e) correspond to copper foam heater surface, respectively. (a-b) show the average bubble count increases in DB regime and decreases in the BIC regime. (d-e) show the average bubble size increases steadily with heat flux. The open and closed symbols in (a-b, d-e) correspond to the training and testing data, respectively. The red symbols correspond to the CHF regime. (c, f) New physical descriptors from the PCA method where (c) the dominant frequency, $D_f$, increases in the DB regime and then decreases in the BIC regime and (f) the amplitude of dominant frequency, $D_a$, increases steadily with heat flux. The circle and triangle symbols in (c, f) correspond to plain copper and copper foam surfaces, respectively. The error bars represent the standard deviation.

Figs. 8a and 8b show the bubble count measured using the supervised Mask R-CNN model for in-house boiling experiments performed on plain Cu and Cu foam surfaces, respectively. Figs. 8d and 8e show the bubble size measured using the same Mask R-CNN model for the same in-house experiments. The bubble count shows an increasing trend within the DB regime until reaching a peak and then steadily decreases when the bubbles start to interfere and coalesce with each other. However, the bubble size shows a steadily increasing trend, where bubble images at higher heat flux result in large standard deviations due to difficulties in the Mask R-CNN's manual bubble tagging task. The difficulty in manual tagging arises due to vigorous bubble coalescence events and inability to accurately segment each individual bubble. The observed trends are consistent with studies that used the Mask R-CNN method to extract bubble count and size [43]. It is noted that the differences between the bubble count/size of CHF and pre-CHF regimes are within the error bars of the analyzed quantities. As such, the bubble count and size are not sufficient to be used as an indicator of the CHF regime and a more robust indicator is in need for reliable boiling crisis detection.

Figs. 8c and 8f show the new physical descriptors, viz.: the dominant frequency, $D_f$, and amplitude, $D_a$, extracted using the PCA method, with circle and triangle symbols corresponding to plain Cu and Cu foam surfaces, respectively. The standard deviations in $D_f$ and $D_a$ at each heat flux are calculated using 10 subsets, each containing 0.5 s images at 1000 fps, from a total of 5000 images. The dominant frequency increases within the DB regime until reaching a peak and then decreases steadily as the heat flux is increased within the BIC regime. Surprisingly, the CHF dataset shows a significantly higher dominant frequency, $D_f$, compared to the near CHF datasets. The red symbols in Fig. 8 correspond to CHF regime. In contrast, the CHF dataset showed a significantly lower amplitude, $D_a$, compared to the near CHF datasets. Differences in bubble dynamics were observed at heat flux values below the CHF point and at the CHF (see SI [91] for videos): (i) the time taken for the bubble to grow and depart from the heater surface is much reduced for CHF compared to pre-CHF, resulting in a dominant frequency increase at CHF than pre-CHF (Fig. 8c), (ii) the bubble size at CHF is smaller than pre-CHF, demonstrated by a clear decrease in amplitude of the dominant frequency (Fig. 8f). The same behavior cannot be distinctly observed in Mask R-CNN's average bubble size results due to its challenge at capturing bubble statistics when the bubble morphology is complex and chaotic. Based on the obvious changes in $D_f$ and $D_a$ values for bubble images before CHF and at CHF, these two new physical descriptors can be utilized as excellent indicators of the boiling crisis.

A qualitative comparison of the results obtained from the supervised Mask R-CNN and the unsupervised PCA approach reveals several similarities, viz., (a) the increasing trend of the bubble count and $D_f$ within the DB regime and their steady decrease within the BIC regime and (b) the increasing trend of the bubble size and $D_a$ within the DB and BIC regimes. The above similarities suggest that (i) the bubble count and the dominant frequency and (ii) the bubble size and the amplitude could be related to each other. Based on the above observations, it is reasonable to interpret that the PCA results encode the bubble count and size information found in the boiling images. Even though the bubble count and size extracted from Mask R-CNN versus heat flux trends show measurable differences in the DB and BIC regime, their values are unreliable when the task is to distinguish the BIC and CHF regimes. The PCA approach does not need any human supervision (no data labeling, bubble tagging, etc.) and shows clear dominant frequency trends at DB, BIC, and CHF regimes, and the new physical descriptors at different heat flux values can then be used to determine the boil-

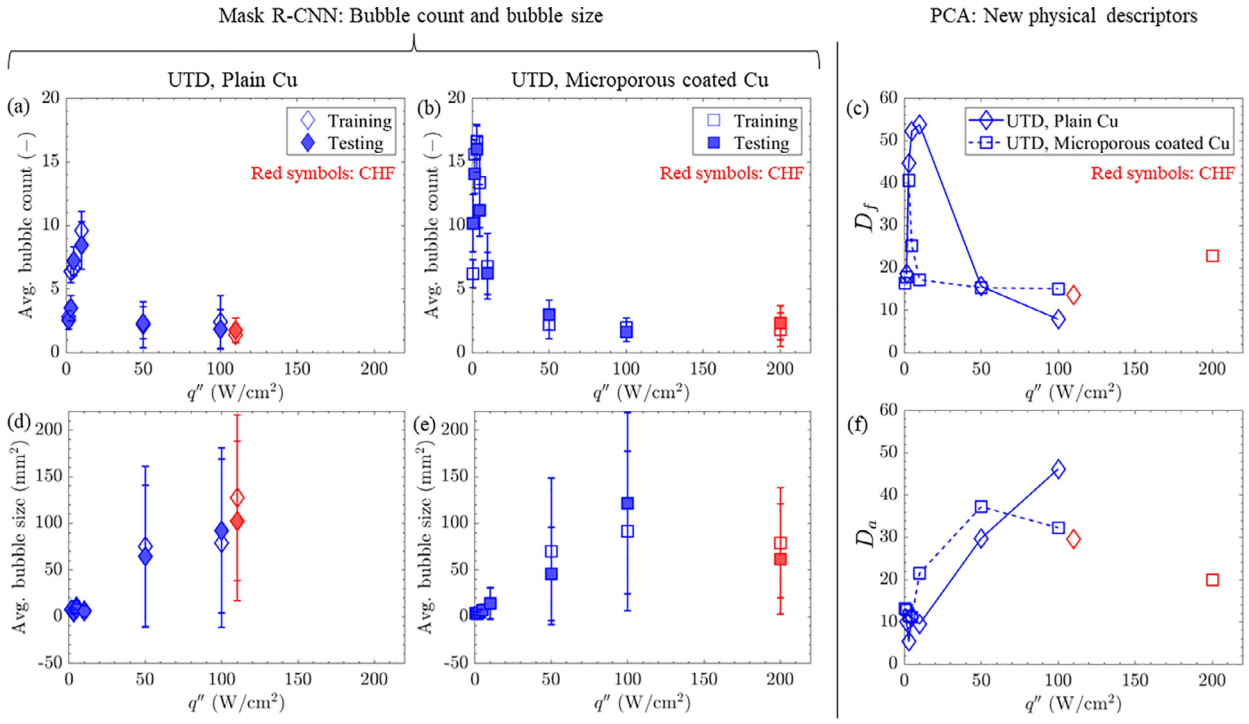


**Fig. 9.** A qualitative comparison of the results obtained from the supervised Mask R-CNN and the unsupervised PCA approach, for publicly available dataset [73]. (a-b, d-e) Bubble count and size calculated using Mask R-CNN with increasing heat flux where (a, d) correspond to plain copper heater surface and (b, e) correspond to microporous coated copper heater surface, respectively. (a-b) show the average bubble count increases in DB regime and decreases in the BIC regime. (d-e) show the average bubble size increases steadily with heat flux. The open and closed symbols in (a-b, d-e) correspond to the training and testing data, respectively. The red symbols correspond to the CHF regime. (c, f) New physical descriptors from PCA method where (c) the dominant frequency, $D_f$, increases in the DB regime and then decreases in the BIC regime and (f) the amplitude of dominant frequency, $D_a$, increases steadily with heat flux. The diamond and square symbols in (c, f) correspond to plain copper and microporous coated copper surfaces, respectively. The error bars in (a-b, d-e) represent the standard deviation, however, standard deviations are not shown in PCA results (c, f) due to a limited number of images available in public dataset [73].

ing regimes of the bubble images with much higher accuracy compared to the bubble count and size.

To examine the robustness of the PCA approach on datasets from various domains, we applied the PCA approach on a publicly available dataset [73] to verify the new physical descriptors encoded by PCA, and obtained consistent results. Fig. 9 compares the bubble count and size of publicly available boiling datasets [73], with Figs. 9a and 9d for a plain Cu heater surface and Figs. 9b and 9e for a microporous coated Cu heater surface, respectively. Fig. 9c shows the dominant frequency, $D_f$, and its associated amplitude, $D_a$, is in Fig. 9f. Figs. 9a-b and 9d-e show the average bubble count and average bubble size at different heat fluxes, respectively. The average bubble count and dominant frequency exhibit an increasing-decreasing trend, while average bubble size and amplitude show an increasing trend as heat flux increases. The results also show that the behaviors of $D_f$ and $D_a$ when the heat flux reaches the CHF point are consistent with the ones shown in Figs. 8c and 8f, respectively. The red symbols in Fig. 9 correspond to the CHF regime. Based on the above findings, the results from the PCA approach show that the unsupervised ML method can encode the bubble morphologies directly from the images, such that the PCA results can be successfully interpreted. The results from the PCA approach can also be used to detect the transition from DB to BIC and BIC to CHF, with minimal human supervision, using the trends of dominant frequency and its associated amplitude.

### *3.2. Future boiling image prediction using PCA-BiLSTM: Steady-State boiling*

The time-series PC data extracted from the bubble images at CHF were used to train the BiLSTM model and the training details are explained in Section 2.3. Fig. 10a shows the RMSE value for the first 10 PCs, where the average and standard deviations were calculated from 10 trials for each PC. The average value of RMSE gradually decreases for higher rank PCs since they encode less information compared to the first few PCs. Out of the 10 trials, the model with the least RMSE value was selected to predict future PC versus time data. Figs. 10b and 10c show the performance of the best trained BiLSTM model in predicting the 1st and 10th PC, respectively, over the next 100 ms (3027 to 3,127 ms) based on 200 ms (2827 to 3,027 ms) of input data, where blue and red symbols correspond to the input and predicted PC values, respectively. The comparison of predicted and input PCs (Figs. 10b and 10c) shows good accuracy of DL model to learn time-series variations of PCs and the predicted PCs can be used to represent the bubble dynamics during pool boiling using the reduced-order representation of bubble images.

The performance of the DL model is evaluated by comparing the predicted and true reduced-order bubble images. Fig. 11 shows a comparison between the true full resolution future image, $U(x)$ (first panel), the true reduced-order future image, $u(x)$ (second panel), the predicted reduced-order future image, $\widehat{u}(x)$ (third panel), and the modified point-wise absolute error $\frac{|u(x)-\widehat{u}(x)|}{\max(|u(x)-\widehat{u}(x)|)}$ (fourth panel), respectively, for an image from the CHF dataset. Here, the denominator, $\max(|u(x)-\widehat{u}(x)|)$, is calculated based on the entire time-series prediction from 3027 to 3,127 ms (100 ms). The modified point-wise absolute error for the prediction is calculated by rescaling the point-wise absolute error between 0 and 1 over the entire time-series prediction. The error analysis presented above only compares the pixel-by-pixel intensity value and does not account for the structural similarity between the true and pre-

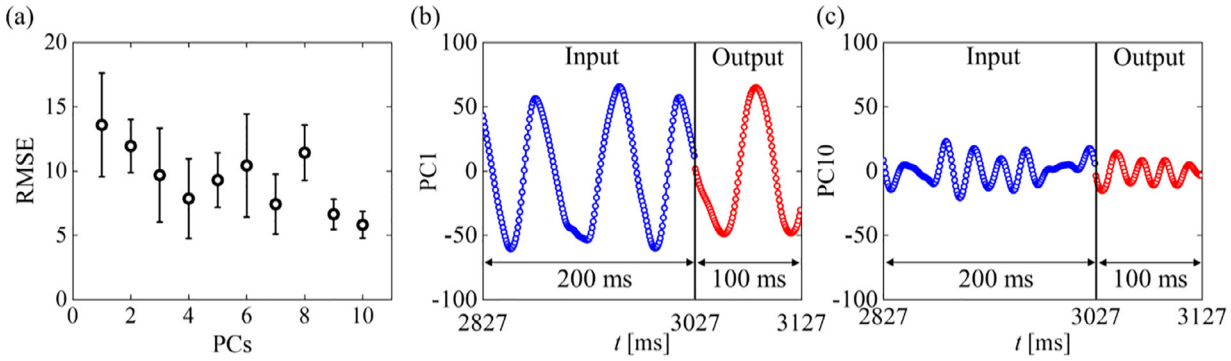


**Fig. 10.** (a) The RMSE value for the first 10 PCs, where there are 10 trials for each PC BiLSTM training. (b) The comparison of the input and predicted PC1, where the red and blue symbols correspond to output and input PC. Here, 200 frames, corresponding to 0.2 s (2827 to 3,027 ms) are used as input to the BiLSTM model, results in output of 0.1 s (3027 to 3,127 ms). (c) Comparison of input and predicted PC10.

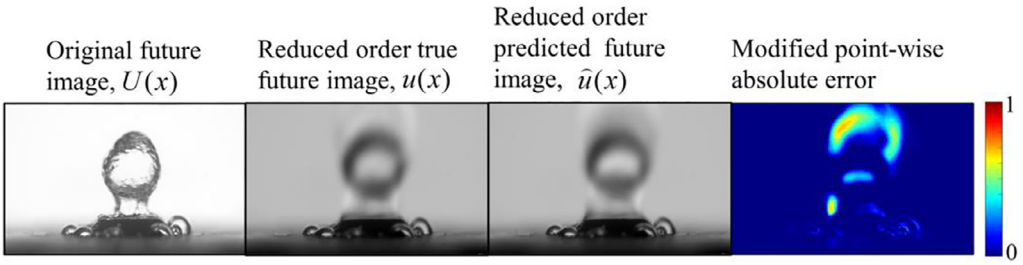


**Fig. 11.** The true image captured during boiling, the reduced-order form of the image, and the reduced-order form of the predicted image are shown. The point-wise absolute error is calculated between reduced-order true and predicted image. The SSIM value calculated using reduced-order true future image and the reduced-order predicted future image was 0.994.

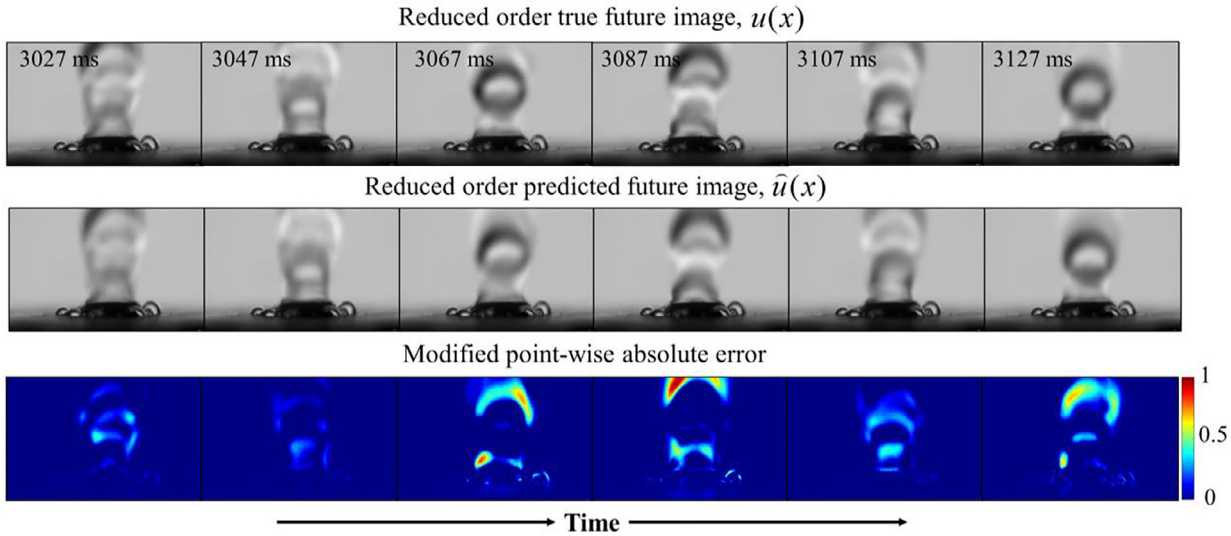


**Fig. 12.** Comparison of bubble dynamics between reduced-order true and predicted using BiLSTM with the modified point-wise absolute error for CHF (109.9 W/cm$^2$). The average SSIM value calculated using reduced-order true future images and the reduced-order predicted future images was 0.995 with a standard deviation of 0.003.

dicted reduced-order future images. The maximum value of modified point-wise absolute error (Fig. 11, fourth panel) was 0.71. To quantify the structural similarity, structural similarity index measure (SSIM) is calculated for all the images. For the reduced-order true future image $u(x)$, and reduced order predicted future image $\hat{u}(x)$, the SSIM value was 0.994, suggesting that both the true and predicted reduced-order images have significant similarities with respect to the bubble morphologies.

Fig. 12 shows a comparison between the true reduced-order future image, the predicted reduced-order future image, and the modified point-wise absolute error, respectively, for bubble images at 3027, 3047, 3067, 3087, 3107, and 3127 ms, taken within the prediction timeframe of 3027 to 3127 ms for CHF. SSIM was calculated over the entire prediction duration (3027 to 3127 ms), where the average and standard deviation were 0.995 and 0.003, respectively.

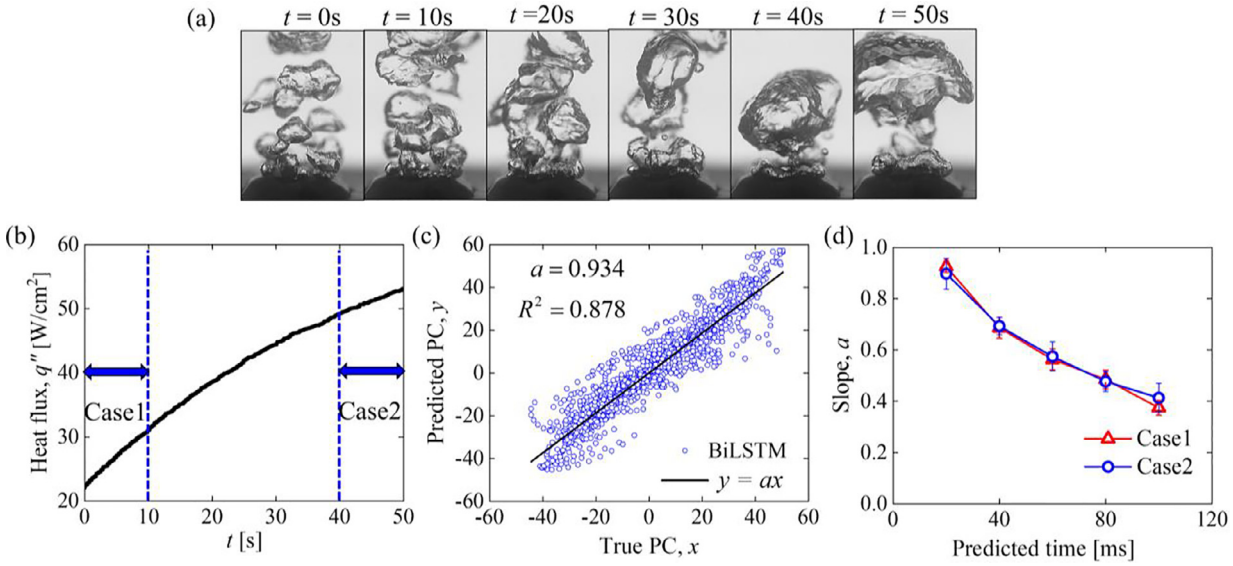


**Fig. 13.** (a) True images of bubble dynamics during the transient heat ramp-up. (b) Transient heat flux during the 50 s time, where Case 1 (first 10 s) and Case 2 (last 10 s) are considered for performance evaluation. (c) Comparison of BiLSTM predicted and True PC for Case 1 of prediction time of 20 ms shows slope, $a = 0.934$. Here, slope is calculated from the best fitted line, black line. (d) The slope, $a$ vs. predicted time shows higher accuracy for shorter prediction.

### *3.3. Future boiling image prediction using PCA-BiLSTM: Transient boiling*

The PCA-BiLSTM is also tested on a transient boiling dataset to demonstrate the capability of the DL model in predicting transient bubble dynamics. The goal here is to train a BiLSTM DL model that can predict the reduced-order images which can be correlated with a heat flux value. Since the heat flux of the true future image is known, the predicted future image can then be associated with a predicted heat flux value, thereby enabling the detection of a boiling crisis. Fig. 13a shows the true images of bubble dynamics during the transient boiling experiment where the heat flux varies from 22.1 W/cm$^2$ to 53.1 W/cm$^2$. As seen from the image panels in Fig. 13a, vigorous bubble coalescence was observed as the heat flux increases. Fig. 13b shows the heat flux versus time, measured using the thermocouples during the 50 s heat flux ramp up. Instead of focusing on the entire 50 s data, where the variations of the bubble dynamics are significantly large for BiLSTM training, we focused on more simplified cases of 10 s data to estimate the trained model performance. Two different cases are considered for performance evaluation of BiLSTM, Case 1 using first 10 s data and Case 2 using last 10 s data, as shown in Fig. 13b. For each case, 10 s of data, where 70% (7 s) of the data are reserved for the BiLSTM training and the remaining 30% (3 s) data are used for the testing. To test the trained BiLSTM model's accuracy on predicting the future of the reduced-order images, the model was set up to predict 20, 40, 60, 80, and 100 ms future reduced-order images. For all the cases, input time to the model was fixed at 200 ms. Fig. 13c compares the BiLSTM predicted PC1 with the true PC1 for Case 1 with 20 ms of prediction duration using the 3 s of testing data. A best fitted line (black line) passing through the origin was plotted to obtain the slope, $a$, as shown in Fig. 13c. The slope, $a$ is 0.934, where a slope,$a \rightarrow 1$ corresponds to perfect prediction and $a \rightarrow 0$ corresponds to poor prediction. Fig. 13d shows the variation of slope, $a$ with respect to prediction duration. The decrease of slope demonstrates that the prediction accuracy decreases with the increase in prediction duration. Fig. 13d also demonstrates the potential universality of the trained BiLSTM model for different heat flux ramping rates. In Case 1 of Fig. 13b, the heat flux increases from 22.55 to 32.67 W/cm$^2$ in 10 s, which corresponds to a ramping rate of 1.011 W/cm$^2$ per second. For Case 2, the heat flux increases from 52.33 to 56.14 W/cm$^2$ in 10 s, corresponding to a ramping rate of 0.381 W/cm$^2$ per second, 38% of that in Case 1. The red and blue symbols in Fig. 13d show the performance of the trained BiLSTM model for both cases in future prediction. The trained BiLSTM models show similar prediction accuracies for both cases, demonstrating the potential universality of the trained BiLSTM models. It is noted that the current BiLSTM model predicts the imminent frame based on similar heat flux values. To predict the imminent frame corresponding to an increased heat flux, the BiLSTM model needs to be trained and evaluated by sampling the PC versus time value at a higher temporal interval. To further investigate the prediction of bubble dynamics, in the present study, the case of 60 ms prediction was used on the Case 1 dataset.

Fig. 14a shows the RMSE value calculated using the testing dataset (2.8 s) for the first 10 PCs for Case 1. The average and error bar were calculated from 10 trials for each PC. Similar to the steady-state case, the best model with minimum RMSE value was selected for the future prediction. Fig. 14b shows the performance of the BiLSTM model in predicting the 1st PC for the next 60 ms based on 200 ms of input data. Here, red, and blue symbols corresponding to predicted and true PC. Fig. 14c shows the comparison of predicted and true 1st PC for the entire testing dataset of 3 s duration, with a prediction window of 60 ms, thereby demonstrating the ability of the trained model to continuously predict the next 60 ms based on previous 200 ms data. Fig. 15 shows the modified point-wise absolute error between the reduced-order true and predicted images from PCA-BiLSTM at 7202, 7220, 7240, and 7,260 ms, taken within the prediction time frame of 60 ms (7,200 ms to 7,260 ms). Similar to the model performance on steady-state data (Fig. 12), the modified point-wise absolute error increases with the prediction duration. The average SSIM value was 0.983 and the standard deviation of SSIM was 0.007.

It is noted that the PCA-BiLSTM approach is a two-step process, where the first step is to calculate the PCs from the boiling images and the second step is to predict future PCs using the BiLSTM model. The PC calculation time from 60 ms of boiling images at full pixel resolution of 600 $\times$ 832 is $\approx$1,097 ms using a single Nvidia Tesla V100 GPU. PC calculation time decreases when the

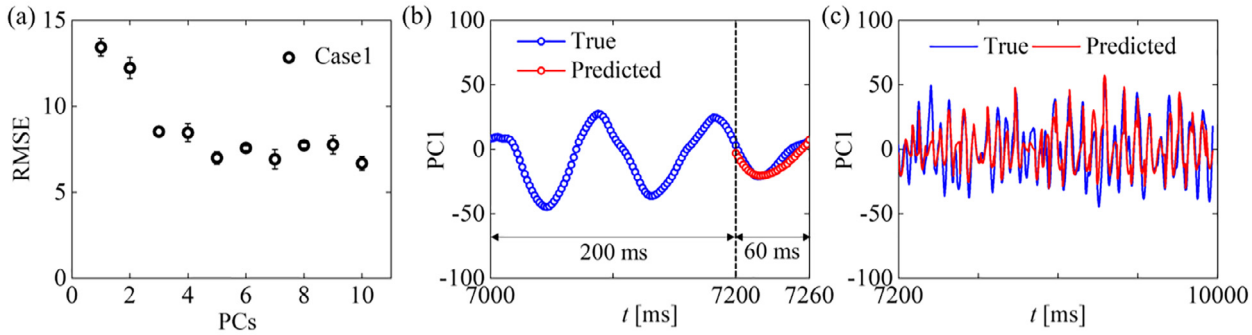


**Fig. 14.** (a) RMSE value calculated between the predicted and the true PCs over the testing dataset (2.8 s). (b) Comparison of true and predicted 1st PC, where red and blue corresponding to predicted and true PC. Here, 200 ms (7,000 ms to 7,200 ms) are used as input to the BiLSTM model, results in output of 60 ms (7,200 ms to 7,260 ms). (c) Comparison of true and BiLSTM predicted PC1 for the entire testing dataset, 2.8 s (7,200 ms to 10,000 ms), having the prediction window of 60 ms.

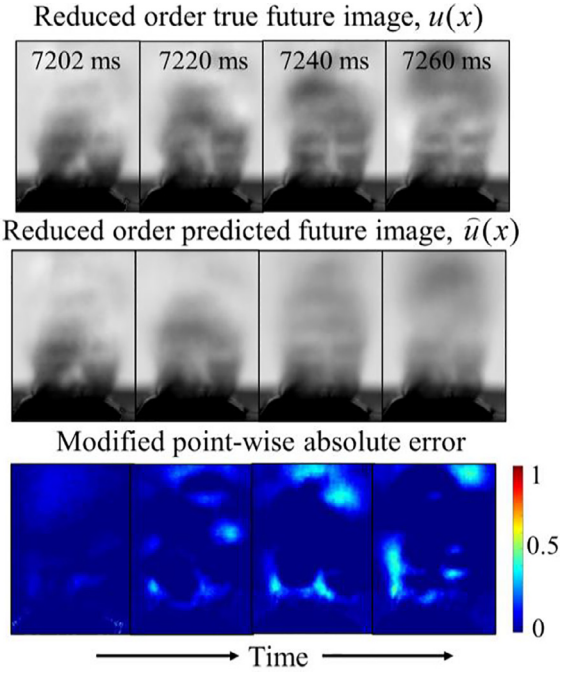


**Fig. 15.** Reduced-order true bubble dynamics for the transient dataset (Case 1) using first 10 PCs (top row), predicted reduced-order bubble dynamics, constructed using BiLSTM predicted PCs (middle row), and the modified point-wise absolute error, calculated between reduced-order true and predicted images (bottom row). The average SSIM value calculated using reduced-order true future images and the reduced-order predicted future images was 0.983 with a standard deviation of 0.007.

image resolution is reduced, and the PC extraction time reduces to ≈16.72 ms when 10% of the original image resolution is used. Once the PCs are calculated, future PC predictions depend on the trained BiLSTM model and in the present study, it takes ≈12.67 ms to predict the next 60 ms of the first 10 PCs. Hence, the total PC calculation and predict time is ≈29.39 ms for the next 60 ms prediction, based on 10% of the original image resolution, demonstrating the ability of the present PCA-BiLSTM method in real-time CHF monitoring and prediction. In addition, PC calculation and prediction time can be further reduced using multiple GPUs to speed up the process.

To demonstrate that the current PCA-BiLSTM method performs significantly better at predicting future bubble dynamics compared to the conventional Convolutional-LSTM (Conv-LSTM) method, both methods were used on the transient boiling dataset (Case 1) shown in Fig. 13a. Conv-LSTM uses the convolution operation by applying equal significance to all the pixels for future prediction, and the prediction results are influenced by the stationary bubbles, heater surface, as well as the image background. In contrast to the Conv-LSTM approach, the present PCA-BiLSTM approach focuses only on the dynamic part of time-series images for future predictions, i.e., the bubble dynamics. Moreover, PCA-BiLSTM uses the first 10 dominant components for future prediction, whereas Conv-LSTM uses full resolution for each image. PCA-BiLSTM and Conv-LSTM are based on different approaches, where the former is data-driven, and the latter is image-based, respectively. The transient bubble images were used to train and test the performance of Conv-LSTM. Both Conv-LSTM and PCA-LSTM models used 3500 images out of 5000 images for training. For Conv-LSTM model, four 2D Convolutional-LSTM layers with 40 filters of size 3 by 3 were used and the last layer was a 3D convolution layer with 1 filter of size 3 by 3 by 3 with sigmoid activation function. To be consistent with the PCA-BiLSTM, the Conv-LSTM model was trained to predict the next 60 ms, corresponding to 30 frames (500 fps). Fig. 16a shows the original future images in the top row and predicted future images using Conv-LSTM in the middle row at 7202, 7220, 7240, and 7,260 ms, taken within the prediction window of 60 ms (7200 to 7,260 ms). The modified point-wise absolute error increases as the prediction duration increased, where the denominator is the maximum value taken within 60 ms and was kept constant. Fig. 16b shows the comparison of average absolute error, avg.$|u(x) - \widehat{u}(x)|$, within the prediction time frame of 60 ms (7200 to 7,260 ms) for PCA-BiLSTM (black circles) and Conv-LSTM (blue circles), respectively. Comparison of time-series average absolute errors in Fig. 16b demonstrates that the PCA-BiLSTM approach outperforms Conv-LSTM in predicting future bubble dynamics. The average absolute error for PCA-BiLSTM is smaller than the Conv-LSTM and the propagation of error with prediction time is much higher for Conv-LSTM. The structural similarity of the images (SSIM) predicted using PCA-BiLSTM and Conv-LSTM are shown in Fig. 16c [92]. As seen from Fig. 16c, the SSIM values of PCA-BiLSTM predictions are significantly higher than that of Conv-LSTM predictions, suggesting that the true and predicted future images from PCA-LSTM had more comparable features and the ones from Conv-LSTM had significant deviations.

The DL model training time was also compared between PCA-BiLSTM and Conv-LSTM. The model training times were 1,497 s/epoch and 59,710 s/epoch for PCA-BiLSTM and Conv-LSTM, respectively, using an Nvidia P4000 GPU. The training time was also checked using an advanced GPU, Nvidia Tesla V100, where the model training times were 362 s/epoch and 512 s/epoch for PCA-BiLSTM and Conv-LSTM, respectively. For both cases, a single GPU was used. The reason for such differences may be due to advanced GPUs' ability to handle a large number of images.

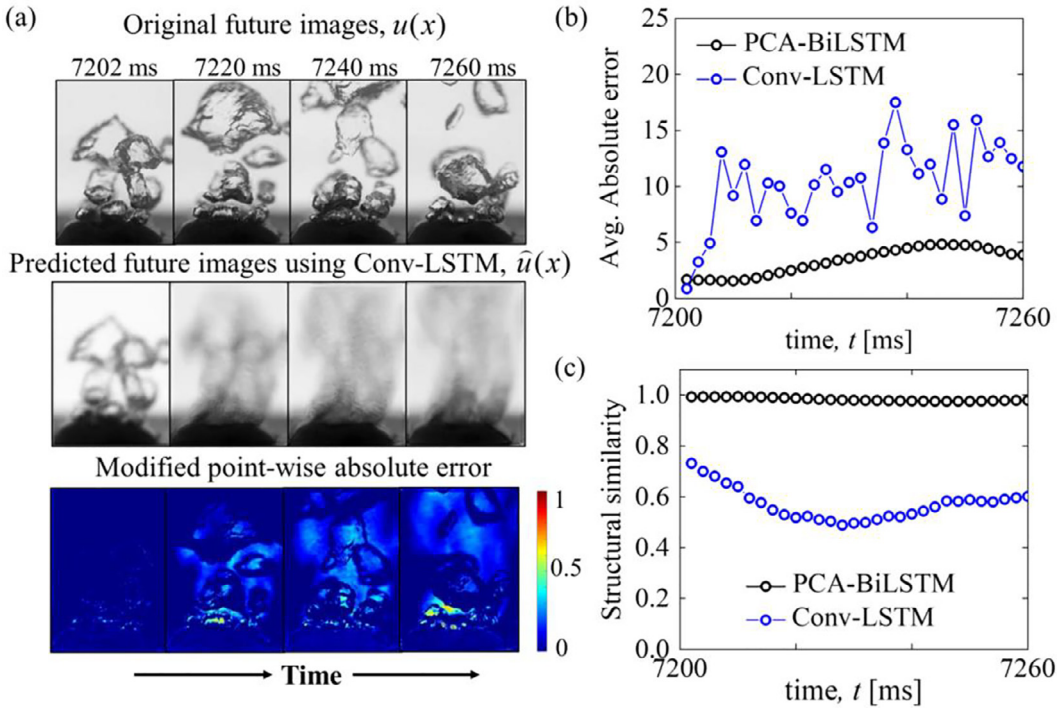


**Fig. 16.** (a) Comparison of bubble dynamics between the original images (top row) and the predicted image using Conv-LSTM (middle row), with the modified point-wise absolute error (bottom row) for the transient dataset of pool boiling on plain Cu. (b) Comparison of average absolute error within the prediction time frame of 60 ms (7200 ms to 7260 ms), where the black and blue symbols are for PCA-BiLSTM and Conv-LSTM for CHF dataset. Here, Average absolute error, avg. $|u(x) - \bar{u}(x)|$, was calculated from original images ($u(x)$) and the predicted images from Conv-LSTM ($\hat{u}(x)$) for Conv-LSTM and using reduced-order true ($u(x)$) and predicted from BiLSTM ($\bar{u}(x)$) for PCA-BiLSTM. (c) Comparison of structural similarity index (SSIM) [92] between PCA-BiLSTM and Conv-LSTM.

## 4. Conclusion

A Principal Component Analysis (PCA) based unsupervised machine learning method was applied on boiling images obtained from in-house pool boiling experiments as well as publicly available videos. The PCA was used to create reduced-order representations of full-resolution images and differentiate significant features from insignificant stationary image regions and noise. Images captured over the duration of bubble generation and departure were represented with as low as 10 principal components (PCs) and the variation of the first PC versus time was analyzed using Fast Fourier Transform (FFT) to extract the new physical descriptors; dominant frequency and amplitude. The results show that:

- The dominant frequency versus heat flux encoded the physical information related to the bubble count observed during the steady-state boiling and the amplitude versus heat flux encoded the physical information related to the bubble size. Within the NB regime, these new physical descriptors showed trends similar to the bubble count and bubble size, however, at CHF, the frequency and amplitude values showed a sudden increase and a sudden decrease, respectively, and can hence be used to distinguish CHF regime from the NB regime during pool boiling experiments.
- The PCA approach was tested on 10 different in-house datasets as well as two publicly available datasets and showed high robustness over multiple domains. Moreover, when the boiling heat flux increased and the bubbles started to interfere and coalesce, the dominant frequency and amplitude versus heat flux trends from PCA showed higher accuracy compared to bubble count and bubble size versus heat flux trends from Mask R-CNN, a supervised learning approach.
- The PC versus time data were then used to train a BiLSTM deep learning model to predict the future states of the PCs. The first 10 PCs were used as input to BiLSTM, and the predicted future PCs were then used to reconstruct the reduced-order images. The error between the predicted and true reduced-order images was found to increase with the prediction duration. The current reduced-order PCA-BiLSTM approach showed significantly higher accuracy compared to Convolutional-LSTM approach in predicting future bubble morphologies, thereby providing a robust pathway for real-time predictions of transient boiling processes.

The present study sheds light on using label-free PCA for reduced-order representations of bubble images to extract new physical descriptors related to the pool boiling phenomena. The PCA-BiLSTM approach is demonstrated to predict future reduced-order bubble images with as few as 10 PCs in comparison to Convolutional-LSTM which relies on high-resolution images containing millions of pixels. The unsupervised PCA combined with the BiLSTM approach presented herein, if integrated with classification-based algorithms [93], has the potential for fast (reduced-order) and domain-independent (robust) detection of the boiling crisis.

## Declaration of Competing Interest

The authors declare that they have no known competing financial interests or personal relationships that could have appeared to influence the work reported in this paper.

## CRediT authorship contribution statement

**Arif Rokoni:** Conceptualization, Data curation, Methodology, Investigation, Software, Visualization, Writing – original draft.

**Lige Zhang:** Data curation, Investigation, Methodology, Visualization. **Tejaswi Soori:** Conceptualization, Investigation, Methodology, Writing – original draft. **Han Hu:** Conceptualization, Data curation, Investigation, Methodology, Writing – review & editing. **Teresa Wu:** Methodology, Writing – review & editing. **Ying Sun:** Conceptualization, Methodology, Writing – review & editing, Supervision, Funding acquisition.

## Acknowledgments

Support for this work was provided in part by the US National Science Foundation under Grant No. CBET-1705745.

## Supplementary materials

Supplementary material associated with this article can be found, in the online version, at doi:10.1016/j.ijheatmasstransfer.2021.122501.

## Appendix A. Training and validation loss of the BiLSTM model

The time-series PC data extracted from the bubble images at CHF were used to train the BiLSTM model. To avoid model overfitting and underfitting issues, 5% of the training dataset was used for validation during the model training. Fig. A1 shows the training and validation loss as a function of the number of epochs, where black and blue symbols correspond to the training and validation datasets. The decreasing trend and good agreement between the training and validation losses indicate a good fit DL model.

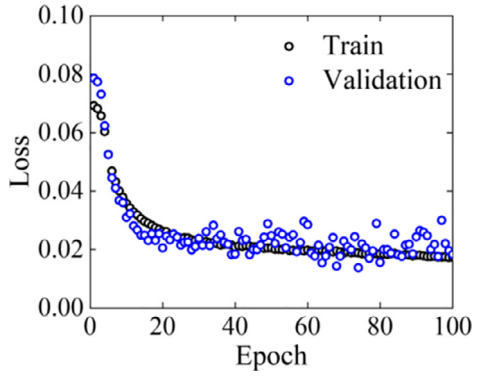


**Fig. A1.** Training and validation loss of the BiLSTM model training.

## Appendix B. Comparison between LSTM and BiLSTM

The prediction performance of BiLSTM was compared with LSTM using the transient boiling dataset, as mentioned in Section 3.3. Figure B1a shows the calculated heat flux during the 50 s transient ramp up. Two different cases were considered for performance evaluation of BiLSTM with traditional LSTM, Case 1 using the first 10 s data and Case 2 using the last 10 s data, as shown in Fig. B1a. For each case, 10 s of data correspond to 5000 images, where 70% (3500) of the data were reserved for LSTM/BiLSTM training and the remaining 30% (1500) were used for testing. For each case, five different numbers of prediction frames, 10, 20, 30, 40 and 50 frames were considered while keeping the same input frames of 100 during training and testing, corresponding to 20, 40, 60, 80, and 100 ms of future prediction using 200 ms of input data. Figures B1b and B1c show the root mean square error (RMSE) value for Case 1 and Case 2, calculated using the true and prediction, where the red symbol is for tradition LSTM and the blue symbol is for BiLSTM. The Figs. B1 (b-c) show that BiLSTM performed better than the traditional LSTM for both cases. The percentage of reduction in RMSE value for future prediction using BiLSTM varies from 5.4% to 15.9% for case 1 and 7.2% to 29.7% for case 2. The average percentage reduction in RMSE value considering all the cases is 15% due to using BiLSTM architecture over traditional LSTM.

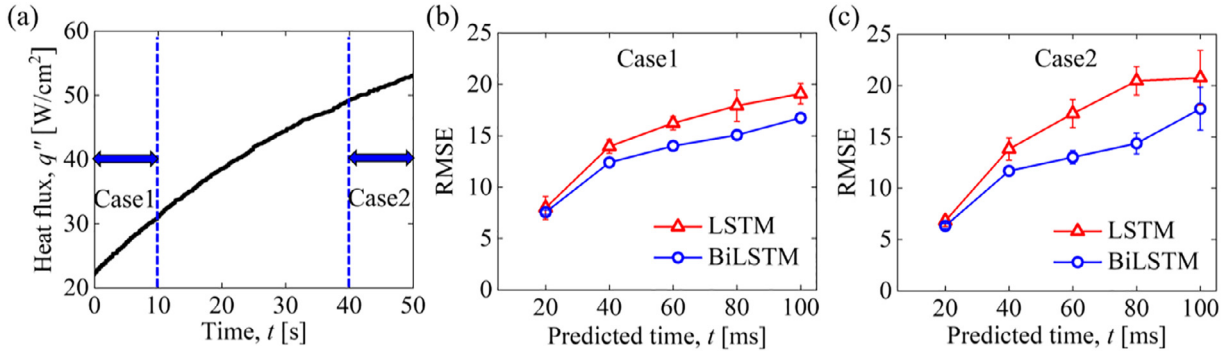


**Fig. B1.** (a) 50 s transient heat flux ramp-up test, where Case 1 (first 10 s) and Case 2 (last 10 s) are considered for performance evaluation. RMSE value with respect to future prediction durations using both LSTM and BiLSTM for (b) Case 1 and (c) Case 2.

## References


[1] J. Dirker, D. Juggurnath, A. Kaya, E.A. Osowade, M. Simpson, S. Lecompte, S.M.A. Noori Rahim Abadi, V. Voulgaropoulos, A.O. Adelaja, M.Z. Dauhoo, Thermal energy processes in direct steam generation solar systems: boiling, condensation and energy storage–a review, Front. Energy Res. 6 (2019) 147.

[2] T.F. Clasen, D.H. Thao, S. Boisson, O. Shipin, Microbiological effectiveness and cost of boiling to disinfect drinking water in rural Vietnam, Environ. Sci. Technol. 42 (12) (2008) 4255–4260.

[3] K.-J. Park, D. Jung, Boiling heat transfer enhancement with carbon nanotubes for refrigerants used in building air-conditioning, Energy Build. 39 (9) (2007) 1061–1064.

[4] P. Birbarah, T. Gebrael, T. Foulkes, A. Stillwell, A. Moore, R. Pilawa-Podgurski, N. Miljkovic, Water immersion cooling of high power density electronics, Int. J. Heat Mass Transf. 147 (2020) 118918.

[5] M.S. El-Genk, Immersion cooling nucleate boiling of high power computer chips, Energy Conver. Manag. 53 (1) (2012) 205–218.

[6] K. Ebrahimi, G.F. Jones, A.S. Fleischer, A review of data center cooling technology, operating conditions and the corresponding low-grade waste heat recovery opportunities, Renew. Sustain. Energy Rev. 31 (2014) 622–638.

[7] H. Fenech, Heat Transfer and Fluid Flow in Nuclear Systems, Elsevier, 2013.

[8] N. Zuber, Hydrodynamic Aspects of Boiling Heat Transfer (thesis), United States Atomic Energy Commission, Technical Information Service, 1959.

[9] J. Lienhard, V. Dhir, Hydrodynamic prediction of peak pool-boiling heat fluxes from finite bodies, J. Heat Transfer 95 (2) (1973) 152–158.

[10] T.G. Theofanous, T.-.N. Dinh, High heat flux boiling and burnout as microphysical phenomena: mounting evidence and opportunities, Multiphase Sci. Technol. 18 (3) (2006) 251–276.

[11] K.-.H. Chu, Y. Soo Joung, R. Enright, C.R. Buie, E.N. Wang, Hierarchically structured surfaces for boiling critical heat flux enhancement, Appl. Phys. Lett. 102 (15) (2013) 151602.

[12] S.G. Kandlikar, A theoretical model to predict pool boiling CHF incorporating effects of contact angle and orientation, J. Heat Transfer 123 (6) (2001) 1071–1079.

[13] A.R. Betz, J. Xu, H. Qiu, D. Attinger, Do surfaces with mixed hydrophilic and hydrophobic areas enhance pool boiling? Appl. Phys. Lett. 97 (14) (2010) 141909.

[14] M.M. Rahman, E. Olceroglu, M. McCarthy, Role of wickability on the critical heat flux of structured superhydrophilic surfaces, Langmuir 30 (37) (2014) 11225–11234.

[15] H.D. Kim, M.H. Kim, Effect of nanoparticle deposition on capillary wicking that influences the critical heat flux in nanofluids, Appl. Phys. Lett. 91 (1) (2007) 014104.

[16] M. Tetreault-Friend, R. Azizian, M. Bucci, T. McKrell, J. Buongiorno, M. Rubner, R. Cohen, Critical heat flux maxima resulting from the controlled morphology of nanoporous hydrophilic surface layers, Appl. Phys. Lett. 108 (24) (2016) 243102.

[17] S.G. Liter, M. Kaviany, Pool-boiling CHF enhancement by modulated porous-layer coating: theory and experiment, Int. J. Heat Mass Transf. 44 (22) (2001) 4287–4311.

[18] A. Fazeli, S. Moghaddam, A new paradigm for understanding and enhancing the critical heat flux (CHF) limit, Sci. Rep. 7 (1) (2017) 1–12.

[19] S. Gong, L. Zhang, P. Cheng, E.N. Wang, Understanding triggering mechanisms for critical heat flux in pool boiling based on direct numerical simulations, Int. J. Heat Mass Transf. 163 (2020) 120546.

[20] V. Nikolayev, D. Chatain, Y. Garrabos, D. Beysens, Experimental evidence of the vapor recoil mechanism in the boiling crisis, Phys. Rev. Lett. 97 (18) (2006) 184503.

[21] N.S. Dhillon, J. Buongiorno, K.K. Varanasi, Critical heat flux maxima during boiling crisis on textured surfaces, Nat. Commun. 6 (1) (2015) 1–12.

[22] A. Zou, S.C. Maroo, Critical height of micro/nano structures for pool boiling heat transfer enhancement, Appl. Phys. Lett. 103 (22) (2013) 221602.

[23] P. Raghupathi, S. Kandlikar, Pool boiling enhancement through contact line augmentation, Appl. Phys. Lett. 110 (20) (2017) 204101.

[24] L. Zhang, J.H. Seong, M. Bucci, Percolative scale-free behavior in the boiling crisis, Phys. Rev. Lett. 122 (13) (2019) 134501.

[25] J. Kim, Review of nucleate pool boiling bubble heat transfer mechanisms, Int. J. Multiphase Flow 35 (12) (2009) 1067–1076.

[26] D.E. Kim, D.I. Yu, D.W. Jerng, M.H. Kim, H.S. Ahn, Review of boiling heat transfer enhancement on micro/nanostructured surfaces, Exp. Therm Fluid Sci. 66 (2015) 173–196.

[27] G.R. Warrier, V.K. Dhir, Heat transfer and wall heat flux partitioning during subcooled flow nucleate boiling—a review, J. Heat Transfer 128 (12) (2006) 1243–1256.

[28] V.K. Dhir, Mechanistic prediction of nucleate boiling heat transfer–achievable or a hopeless task? J. Heat Transfer 128 (1) (2006) 1–12.

[29] G. Huber, S. Tanguy, M. Sagan, C. Colin, Direct numerical simulation of nucleate pool boiling at large microscopic contact angle and moderate Jakob number, Int. J. Heat Mass Transf. 113 (2017) 662–682.

[30] Y. Sato, B. Niceno, Nucleate pool boiling simulations using the interface tracking method: boiling regime from discrete bubble to vapor mushroom region, Int. J. Heat Mass Transf. 105 (2017) 505–524.

[31] G. Liang, I. Mudawar, Pool boiling critical heat flux (CHF)–Part 1: review of mechanisms, models, and correlations, Int. J. Heat Mass Transf. 117 (2018) 1352–1367.

[32] M.S. Hameed, A.R. Khan, A. Mahdi, Modeling a general equation for pool boiling heat transfer, Ad. Chem. Eng. Sci. 2013 (2013).

[33] H.H. Son, S.J. Kim, Role of receding capillary flow correlating nano/micro scale surface roughness and wettability with pool boiling critical heat flux, Int. J. Heat Mass Transf. 138 (2019) 985–1001.

[34] D.E. Kim, D.I. Yu, S.C. Park, H.J. Kwak, H.S. Ahn, Critical heat flux triggering mechanism on micro-structured surfaces: coalesced bubble departure frequency and liquid furnishing capability, Int. J. Heat Mass Transf. 91 (2015) 1237–1247.

[35] N.S. Dhillon, J. Buongiorno, K.K. Varanasi, Critical heat flux maxima during boiling crisis on textured surfaces, Nat. Commun. 6 (2015) 8247.

[36] M. Shoji, Studies of boiling chaos: a review, Int. J. Heat Mass Transf. 47 (6–7) (2004) 1105–1128.

[37] D. Groenveld, Heat transfer phenomena related to the boiling crisis, Atomic Energy Canada Ltd (1981).

[38] J. Ortiz-Villafuerte, R. Castillo-Durán, H. Hernández-López, E. Araiza-Martínez, in: Fundamentals of Boiling Water Reactor Safety Design and Operation, in: Towards a Cleaner Planet, Springer, 2007, pp. 123–146.

[39] G.M. Hobold, A.K. da Silva, Machine learning classification of boiling regimes with low speed, direct and indirect visualization, Int. J. Heat Mass Transf. 125 (2018) 1296–1309.

[40] G.M. Hobold, A.K. da Silva, Automatic detection of the onset of film boiling using convolutional neural networks and Bayesian statistics, Int. J. Heat Mass Transf. 134 (2019) 262–270.

[41] G.M. Hobold, A.K. da Silva, Visualization-based nucleate boiling heat flux quantification using machine learning, Int. J. Heat Mass Transf. 134 (2019) 511–520.

[42] M. Ravichandran, M. Bucci, Online, quasi-real-time analysis of high-resolution, infrared, boiling heat transfer investigations using artificial neural networks, Appl. Therm. Eng. 163 (2019) 114357.

[43] Y. Suh, R. Bostanabad, Y. Won, Deep learning predicts boiling heat transfer, Sci. Rep. 11 (1) (2021) 1–10.

[44] M. Ravichandran, G. Su, C. Wang, J.H. Seong, A. Kossolapov, B. Phillips, M.M. Rahman, M. Bucci, Decrypting the boiling crisis through data-driven exploration of high-resolution infrared thermometry measurements, Appl. Phys. Lett. 118 (25) (2021) 253903.

[45] S.M. Rassoulinejad-Mousavi, F. Al-Hindawi, T. Soori, A. Rokoni, H. Yoon, H. Hu, T. Wu, Y. Sun, Deep learning strategies for critical heat flux detection in pool boiling, Appl. Therm. Eng. 190 (2021) 116849.

[46] K.N.R. Sinha, V. Kumar, N. Kumar, A. Thakur, R. Raj, Deep learning the sound of boiling for advance prediction of boiling crisis, Cell Rep. Phys. Sci. 2 (3) (2021) 100382.

[47] X. Liang, Y. Xie, R. Day, X. Meng, H. Wu, A data driven deep neural network model for predicting boiling heat transfer in helical coils under high gravity, Int. J. Heat Mass Transf. 166 (2021) 120743.

[48] T. Cong, R. Chen, G. Su, S. Qiu, W. Tian, Analysis of CHF in saturated forced convective boiling on a heated surface with impinging jets using artificial neural network and genetic algorithm, Nucl. Eng. Des. 241 (9) (2011) 3945–3951.

[49] M. Hassanpour, B. Vaferi, M.E. Masoumi, Estimation of pool boiling heat transfer coefficient of alumina water-based nanofluids by various artificial intelligence (AI) approaches, Appl. Therm. Eng. 128 (2018) 1208–1222.

[50] Y. Liu, N. Dinh, Y. Sato, B. Niceno, Data-driven modeling for boiling heat transfer: using deep neural networks and high-fidelity simulation results, Appl. Therm. Eng. 144 (2018) 305–320.

[51] L. Zhou, D. Garg, Y. Qiu, S.-.M. Kim, I. Mudawar, C.R. Kharangate, Machine learning algorithms to predict flow condensation heat transfer coefficient in mini/micro-channel utilizing universal data, Int. J. Heat Mass Transf. 162 (2020) 120351.

[52] Y. Qiu, D. Garg, L. Zhou, C.R. Kharangate, S.-.M. Kim, I. Mudawar, An artificial neural network model to predict mini/micro-channels saturated flow boiling heat transfer coefficient based on universal consolidated data, Int. J. Heat Mass Transf. 149 (2020) 119211.

[53] Y. Qiu, D. Garg, S.-.M. Kim, I. Mudawar, C.R. Kharangate, Machine learning algorithms to predict flow boiling pressure drop in mini/micro-channels based on universal consolidated data, Int. J. Heat Mass Transf. 178 (2021) 121607.

[54] H. Alimoradi, M. Shams, Optimization of subcooled flow boiling in a vertical pipe by using artificial neural network and multi objective genetic algorithm, Appl. Therm. Eng. 111 (2017) 1039–1051.

[55] T. Cong, G. Su, S. Qiu, W. Tian, Applications of ANNs in flow and heat transfer problems in nuclear engineering: a review work, Prog. Nucl. Energy 62 (2013) 54–71.

[56] J.N. Kutz, S.L. Brunton, B.W. Brunton, J.L. Proctor, Dynamic mode decomposition: data-driven modeling of complex systems, SIAM (2016).

[57] B. Su, Z. Luo, T. Wang, J. Zhang, F. Cheng, Experimental and principal component analysis studies on minimum oxygen concentration of methane explosion, Int. J. Hydrogen Energy 45 (21) (2020) 12225–12235.

[58] Y. Chen, J. Tao, Q. Zhang, K. Yang, X. Chen, J. Xiong, R. Xia, J. Xie, Saliency detection via the improved hierarchical principal component analysis method, Wireless Commun. Mobile Comput. 2020 (2020).

[59] J. Lever, M. Krzywinski, N. Altman, Points of significance: principal component analysis, Nat. Methods 14 (2017) 641–642.

[60] S.J. Wetzel, Unsupervised learning of phase transitions: from principal component analysis to variational autoencoders, Phys. Rev. E 96 (2) (2017) 022140.

[61] M.R. Mahmoudi, M.H. Heydari, S.N. Qasem, A. Mosavi, S.S. Band, Principal component analysis to study the relations between the spread rates of COVID-19 in high risks countries, Alexandria Eng. J. 60 (1) (2021) 457–464.

[62] T. Parhizkar, E. Rafieipour, A. Parhizkar, Evaluation and improvement of energy consumption prediction models using principal component analysis based feature reduction, J. Clean. Prod. 279 (2021) 123866.

[63] R. Vitkovicova, Y. Yokoi, T. Hyhlik, Identification of structures and mechanisms in a flow field by POD analysis for input data obtained from visualization and PIV, Exp. Fluids 61 (8) (2020) 1–21.
[64] W. Lotter, G. Kreiman, D. Cox, arXiv preprint, 2016.
[65] Y. Wang, M. Long, J. Wang, Z. Gao, P.S. Yu, Predrnn: recurrent neural networks for predictive learning using spatiotemporal lstms, in: Proceedings of the 31st International Conference on Neural Information Processing Systems, 2017, pp. 879–888.
[66] Y. Wang, Z. Gao, M. Long, J. Wang, S.Y. Philip, Predrnn++: towards a resolution of the deep-in-time dilemma in spatiotemporal predictive learning, in: International Conference on Machine Learning, PMLR, 2018, pp. 5123–5132.
[67] A.T. Mohan, D.V. Gaitonde, arXiv preprint, 2018.
[68] A. Mohan, D. Daniel, M. Chertkov, D. Livescu, Compressed convolutional LSTM: an efficient deep learning framework to model high fidelity 3D turbulence, 2019 arXiv preprint arXiv:1903.00033.
[69] Z. Deng, Y. Chen, Y. Liu, K.C. Kim, Time-resolved turbulent velocity field reconstruction using a long short-term memory (LSTM)-based artificial intelligence framework, Phys. Fluids 31 (7) (2019) 075108.
[70] K. Hasegawa, K. Fukami, T. Murata, K. Fukagata, CNN-LSTM based reduced order modeling of two-dimensional unsteady flows around a circular cylinder at different Reynolds numbers, Fluid Dyn. Res. 52 (6) (2020) 065501.
[71] P.A. Srinivasan, L. Guastoni, H. Azizpour, P. Schlatter, R. Vinuesa, Predictions of turbulent shear flows using deep neural networks, Phys. Rev. Fluids 4 (5) (2019) 054603.
[72] M.I. Radaideh, C. Pigg, T. Kozlowski, Y. Deng, A. Qu, Neural-based time series forecasting of loss of coolant accidents in nuclear power plants, Expert. Syst. Appl. 160 (2020) 113699.
[73] S.M. You, Pool boiling, https://msht.utdallas.edu/.
[74] S. Jun, J. Kim, S.M. You, H.Y. Kim, Effect of heater orientation on pool boiling heat transfer from sintered copper microporous coating in saturated water, Int. J. Heat Mass Transf. 103 (2016) 277–284.
[75] K. Pearson, LIII, On lines and planes of closest fit to systems of points in space, Lond. Edinbur. Dublin Philos. Mag. J. Sci. 2 (11) (1901) 559–572.
[76] N. Benjamin Erichson, S.L. Brunton, J.Nathan Kutz, Compressed singular value decomposition for image and video processing, in: Proceedings of the IEEE International Conference on Computer Vision Workshops, 2017, pp. 1880–1888.
[77] S. Hochreiter, J. Schmidhuber, Long short-term memory, Neural Comput. 9 (8) (1997) 1735–1780.
[78] S. Selvin, R. Vinayakumar, E. Gopalakrishnan, V.K. Menon, K. Soman, Stock price prediction using LSTM, RNN and CNN-sliding window model, in: 2017 international conference on advances in computing, communications and informatics (icacci), IEEE, 2017, pp. 1643–1647.
[79] Y.-.T. Tsai, Y.-.R. Zeng, Y.-.S. Chang, Air pollution forecasting using RNN with LSTM, in: 2018 IEEE 16th Intl Conf on Dependable, Autonomic and Secure Computing, 16th Intl Conf on Pervasive Intelligence and Computing, 4th Intl Conf on Big Data Intelligence and Computing and Cyber Science and Technology Congress (DASC/PiCom/DataCom/CyberSciTech), IEEE, 2018, pp. 1074–1079.
[80] J. Kumar, R. Goomer, A.K. Singh, Long short term memory recurrent neural network (LSTM-RNN) based workload forecasting model for cloud datacenters, Procedia Comput. Sci. 125 (2018) 676–682.
[81] H. Lu, Z. Ge, Y. Song, D. Jiang, T. Zhou, J. Qin, A temporal-aware lstm enhanced by loss-switch mechanism for traffic flow forecasting, Neurocomputing 427 (2021) 169–178.
[82] A. Sherstinsky, Fundamentals of recurrent neural network (RNN) and long short-term memory (LSTM) network, Phys. D 404 (2020) 132306.
[83] A. Graves, J. Schmidhuber, Framewise phoneme classification with bidirectional LSTM and other neural network architectures, Neural Netw. 18 (5-6) (2005) 602–610.
[84] A. Graves, S. Fernández, J. Schmidhuber, Bidirectional LSTM networks for improved phoneme classification and recognition, in: International conference on artificial neural networks, Springer, 2005, pp. 799–804.
[85] Z. Huang, W. Xu, K. Yu, Bidirectional LSTM-CRF models for sequence tagging, arXiv preprint (2015) arXiv:1508.01991.
[86] E. Marchi, G. Ferroni, F. Eyben, L. Gabrielli, S. Squartini, B. Schuller, Multi-resolution linear prediction based features for audio onset detection with bidirectional LSTM neural networks, in: 2014 IEEE international conference on acoustics, speech and signal processing (ICASSP), IEEE, 2014, pp. 2164–2168.
[87] Y. Fan, Y. Qian, F.-.L. Xie, F.K. Soong, TTS synthesis with bidirectional LSTM based recurrent neural networks, Fifteenth annual conference of the international speech communication association, 2014.
[88] S. Siami-Namini, N. Tavakoli, A.S. Namin, The performance of LSTM and BiLSTM in forecasting time series, in: 2019 IEEE International Conference on Big Data (Big Data), IEEE, 2019, pp. 3285–3292.
[89] W. Abdulla, Mask r-cnn for object detection and instance segmentation on keras and tensorflow, (2017).
[90] Y. Kim, H. Park, Deep learning-based automated and universal bubble detection and mask extraction in complex two-phase flows, Sci. Rep. 11 (1) (2021) 1–11.
[91] doi:10.1016/j.ijheatmasstransfer.2021.122501.
[92] A. Hore, D. Ziou, Image quality metrics: PSNR vs. SSIM, in: 2010 20th international conference on pattern recognition, IEEE, 2010, pp. 2366–2369.
[93] S.B. Kotsiantis, I. Zaharakis, P. Pintelas, Supervised machine learning: a review of classification techniques, Emerg. Artif. Intell. Appl. Comput. Eng. 160 (1) (2007) 3–24.